

Lecture Notes on CMB Theory:
From Nucleosynthesis to Recombination

by
Wayne Hu

arXiv:0802.3688v1 [astro-ph] 25 Feb 2008

Contents

| | | |
|---|--|----|
| CMB Theory from Nucleosynthesis to Recombination | <i>page</i> | 1 |
| 1 | Introduction | 1 |
| 2 | Brief Thermal History | 1 |
| 2.1 | Nucleosynthesis and Prediction of the CMB | 1 |
| 2.2 | Thermalization and Spectral Distortions | 4 |
| 2.3 | Recombination | 6 |
| 3 | Temperature Anisotropy from Recombination | 9 |
| 3.1 | Anisotropy from Inhomogeneity | 10 |
| 3.2 | Acoustic Oscillation Basics | 13 |
| 3.3 | Gravito-Acoustic Oscillations | 18 |
| 3.4 | Baryonic Effects | 22 |
| 3.5 | Matter-Radiation Ratio | 24 |
| 3.6 | Damping | 25 |
| 3.7 | Information from the Peaks | 27 |
| 4 | Polarization Anisotropy from Recombination | 32 |
| 4.1 | Statistical Description | 33 |
| 4.2 | EB Harmonic Description | 34 |
| 4.3 | Thomson Scattering | 35 |
| 4.4 | Acoustic Polarization | 36 |
| 4.5 | Gravitational Waves | 37 |
| 5 | Discussion | 37 |

CMB Theory from Nucleosynthesis to Recombination

1 Introduction

These lecture notes comprise an introduction to the well-established physics and phenomenology of the cosmic microwave background (CMB) between big bang nucleosynthesis and recombination. We take our study through recombination since most of the temperature and polarization anisotropy observed in the CMB formed during the recombination epoch when free electrons became bound into hydrogen and helium.

The other reason for considering only this restricted range from nucleosynthesis to recombination is that these notes are meant to complement the other lectures of the XIX Canary Island Winter School of Astrophysics. While they are self-contained and complete in and of themselves, they omit important topics that will be covered elsewhere in this volume: namely inflation (Sabino Matarrese), observations (Bruce Partridge), statistical analysis (Licia Verde), secondary anisotropy (Matthias Bartelmann), and non-Gaussianity (Enrique Martinez-Gonzalez).

Furthermore the approach taken here of introducing only as much detail as necessary to build physical intuition is more suitable as a general overview rather than a rigorous treatment for training specialists. As such these notes complement the more formal lecture notes for the Trieste school which may anachronistically be viewed as a continuation of these notes in the same notation (Hu 2003).

The outline of these notes are as follows. We begin in §2 with a brief thermal history of the CMB. We discuss the temperature and polarization anisotropy and acoustic peaks from recombination in §3-4 and conclude in §5. We take units throughout with $\hbar = c = k_B = 1$ and illustrate effects in the standard cosmological constant cold dark matter universe with adiabatic inflationary initial conditions (Λ CDM).

2 Brief Thermal History

In this section, we discuss the major events in the thermal history of the CMB. We begin in §2.1 with the formation of the light elements and the original prediction of relic radiation. We continue in §2.2 with the processes that thermalize the CMB into a blackbody. Finally in §2.3, we discuss the recombination epoch where the main sources of temperature and polarization anisotropy lie.

2.1 Nucleosynthesis and Prediction of the CMB

Let us begin our brief thermal history with the relationship between the CMB and the abundance of light elements established at an energy scale of 10^2 keV, time scale of a few minutes, temperature

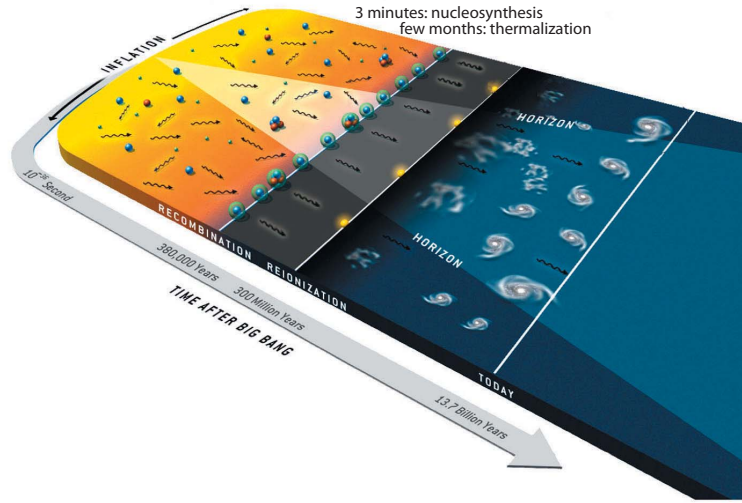


Fig. 1. A brief thermal history: nucleosynthesis, thermalization, recombination and reionization. Adapted from Hu and White (2004).

of 10^9K and redshift of $z \sim 10^8 - 10^9$. This is the epoch of nucleosynthesis, the formation of the light elements. The qualitative features of nucleosynthesis are set by the low baryon-photon number density of our universe. Historically, the sensitivity to this ratio was used by Gamow and collaborators in the late 1940's to predict the existence and estimate the temperature of the CMB. Its modern use is the opposite: with the photon density well measured from the CMB spectrum, the abundance of light elements determines the baryon density.

At the high temperature and densities of nucleosynthesis, radiation is rapidly thermalized to a perfect black body and the photon number density is a fixed function of the temperature $n_\gamma \propto T^3$ (see below). Apart from epochs in which energy from particle annihilation or other processes is dumped into the radiation, the baryon-photon number density ratio remains constant.

Likewise nuclear statistical equilibrium, while satisfied, makes the abundance of the light elements of mass number A follow the expectations of a Maxwell-Boltzmann distribution for the phase space occupation number

$$f_A = e^{-(m_A - \mu_A)/T} e^{-p_A^2/2m_A T}, \quad (1)$$

where p_A is the particle momentum, m_A is the rest mass, and μ_A is the chemical potential. Namely their number density

$$\begin{aligned} n_A &\equiv g_A \int \frac{d^3 p_A}{(2\pi)^3} f_A \\ &= g_A \left(\frac{m_A T}{2\pi} \right)^{3/2} e^{(\mu_A - m_A)/T}. \end{aligned} \quad (2)$$

Here g_A is the degeneracy factor. In equilibrium, the chemical potentials of the various elements are related to those of the proton and neutron by

$$\mu_A = Z\mu_p + (A - Z)\mu_n, \quad (3)$$

where Z is the charge or number of protons. Using this relation, the abundance fraction

$$X_A \equiv A \frac{n_A}{n_b} = A^{5/2} g_A 2^{-A} \left[\left(\frac{2\pi T}{m_b} \right)^{3/2} \frac{2\zeta(3)\eta_{b\gamma}}{\pi^2} \right]^{A-1} e^{B_A/T} X_p^Z X_n^{A-Z}, \quad (4)$$

where X_p and X_n are the proton and neutron abundance, $\zeta(3) \approx 1.202$, and n_b is the baryon number density. The two controlling quantities are the binding energy

$$B_A = Zm_p + (A - Z)m_n - m_A, \quad (5)$$

and the baryon-photon number density ratio $\eta_{b\gamma} = n_b/n_\gamma$. That the latter number is of order 10^{-9} in our universe means that light elements form only well after the temperature has dropped below the binding energy of each species. Nuclear statistical equilibrium holds until the reaction rates drop below the expansion rate. At this point, the abundance freezes out and remains constant.

Gamow's back of the envelope estimate (Gamow 1948, refined by Alpher and Herman 1948) was to consider the neutron capture reaction that forms deuterium



with a binding energy of $B_2 = 2.2\text{MeV}$. Given Eqn. (4)

$$X_2 = \frac{3}{\pi^2} \left(\frac{4\pi T}{m_b} \right)^{3/2} \eta_{b\gamma} \zeta(3) e^{B_2/T} X_p X_n, \quad (7)$$

a low baryon-photon ratio, and $X_n \approx X_p \approx 1/2$ for estimation purposes, the critical temperature for deuterium formation is $T \sim 10^9\text{K}$. In other words the low baryon-photon ratio means that there are sufficient numbers of photons to dissociate deuterium until well below $T \sim B_2$. Note that this condition is only logarithmically sensitive to the exact value of the baryon-photon ratio chosen for the estimate and so the reasoning is not circular.

Furthermore, that we observe deuterium at all and not all helium and heavier elements means that the reaction must have frozen out at near this temperature. Given the thermally averaged cross section of

$$\langle \sigma v \rangle \approx 4.6 \times 10^{-20} \text{cm}^3 \text{s}^{-1}, \quad (8)$$

the freezeout condition

$$n_b \langle \sigma v \rangle \approx H \approx t^{-1}, \quad (9)$$

and the time-temperature relation $t(T = 10^9\text{K}) \approx 180\text{s}$ from the radiation dominated Friedmann equation, we obtain an estimate of the baryon number density

$$n_b(T = 10^9\text{K}) \sim 1.2 \times 10^{17} \text{cm}^{-3}. \quad (10)$$

Comparing this density to the an observed current baryon density and requiring that $n_b \propto a^{-3}$ and $T \propto a^{-1}$ yields the current temperature of the thermal background. For example, taking the modern value of $\Omega_b h^2 \approx 0.02$ and $n_b(a = 1) = 2.2 \times 10^{-7} \text{cm}^{-3}$ yields the rough estimate

$$T(a = 1) \approx 12\text{K}. \quad (11)$$

This value is of the same order of magnitude as the observed CMB temperature 2.725K as well as the original estimates (Alpher and Herman 1948; Dicke et al. 1965). Modern day estimates of the baryon-photon ratio also rely on deuterium (e.g. Tytler et al. 2000). We shall see that the CMB has its own internal measure of this ratio from the acoustic peaks. Agreement between the nucleosynthesis

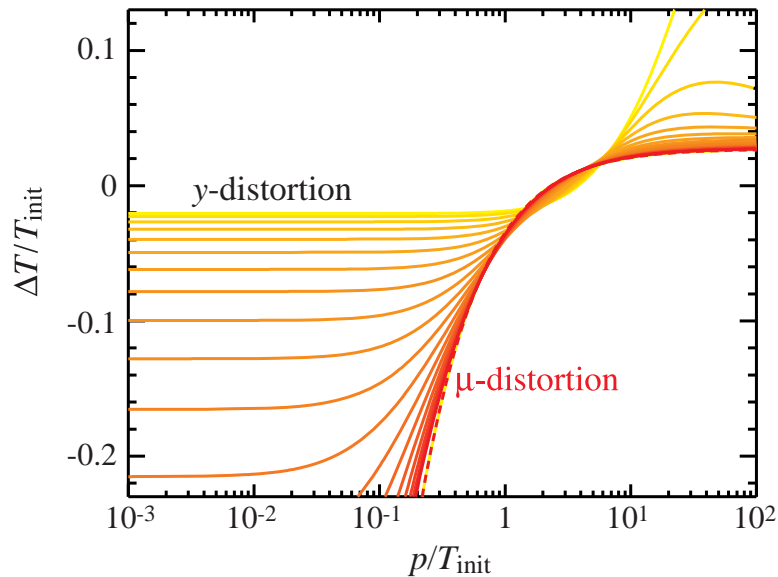


Fig. 2. Comptonization process. Energy injected into the CMB through heating of the electrons is thermalized by Compton scattering. Under the Kompaneets equation, a y -distortion first forms as low frequency photons gain energy from the electrons. After multiple scatterings the distribution is thermalized to a chemical potential or μ -distortion. Adapted from Hu (1995).

and acoustic peak measurements argue that the baryon-photon ratio has not changed appreciably since $z \sim 10^8$.

2.2 Thermalization and Spectral Distortions

Between nucleosynthesis and recombination, processes that create and destroy photons and hence thermalize the CMB fall out of equilibrium. The lack of spectral distortions in the CMB thus constrains any process that injects energy or photons into the plasma after this epoch.

In a low baryon-photon ratio universe, the main thermalization process is double, also known as radiative, Compton scattering

$$e^- + \gamma \leftrightarrow e^- + \gamma + \gamma. \quad (12)$$

The radiative Compton scattering rate becomes insufficient to maintain a blackbody at a redshift of (Danese and de Zotti 1982)

$$z_{\text{therm}} = 2.0 \times 10^6 (1 - Y_p/2)^{-2/5} \left(\frac{\Omega_b h^2}{0.02} \right)^{-2/5} \quad (13)$$

corresponding to a time scale of order a few months.

After this redshift, energy or photon injection appears as a spectral distortion in the spectrum of the CMB. The form of the distortion is determined by Compton scattering

$$e^- + \gamma \leftrightarrow e^- + \gamma, \quad (14)$$

since it is still sufficiently rapid compared with respect to the expansion while hydrogen remains ionized. Because a blackbody has a definite number density of photons at a given temperature,

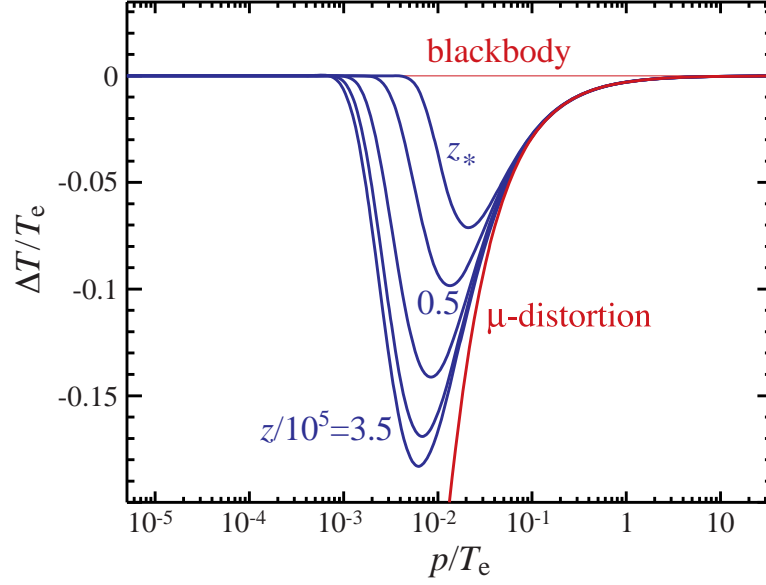


Fig. 3. Low frequency thermalization by bremsstrahlung. Creation and absorption of photons at low frequencies by bremsstrahlung bring a chemical potential distortion back to blackbody at the electron temperature T_e between z_K and recombination. Adapted from Hu and Silk (1993).

energy exchange via Compton scattering alone can only produce a Bose-Einstein spectrum for the photon distribution function

$$f = \frac{1}{e^{(E-\mu)/T} - 1} \quad (15)$$

with μ determined by the conserved number density and temperature. The evolution to a Bose-Einstein distribution is determined by solving the Kompaneets equation (Zeldovich and Sunyaev 1969). The Kompaneets equation is Boltzmann equation for Compton scattering in a homogeneous medium. It includes the effects of electron recoil and the second order Doppler shift that exchange energy between the photons and electrons. If energy is injected into the plasma to heat the electrons, Comptonization will try to redistribute the energy to the CMB. Consequently the first step in Comptonization is a so called “ y distortion” in the spectrum as low energy photons in the Rayleigh Jeans tail of the CMB gain energy from the second order Doppler shift (see Fig. 2).

After multiple scatterings, the spectrum settles into the Bose-Einstein form with a “ μ distortion.” The transition occurs when the energy-transfer weighted optical depth approaches unity, *i.e.* $\tau_K(z_K) = 4 \int dt n_e \sigma_T T_e / m_e = 1$ where n_e is the electron density σ_T is the Thomson cross section, T_e is the electron temperature and m_e is the electron mass

$$z_K \approx 5.1 \times 10^4 (1 - Y_p/2)^{-1/2} \left(\frac{\Omega_b h^2}{0.02} \right)^{-1/2}. \quad (16)$$

Above this redshift energy injection creates a μ distortion, below a y distortion.

At very low frequencies, bremsstrahlung

$$e^- + p \leftrightarrow e^- + p + \gamma \quad (17)$$

is still efficient in creating and absorbing photons. In Fig. 3 we show the how a μ -distortion continues

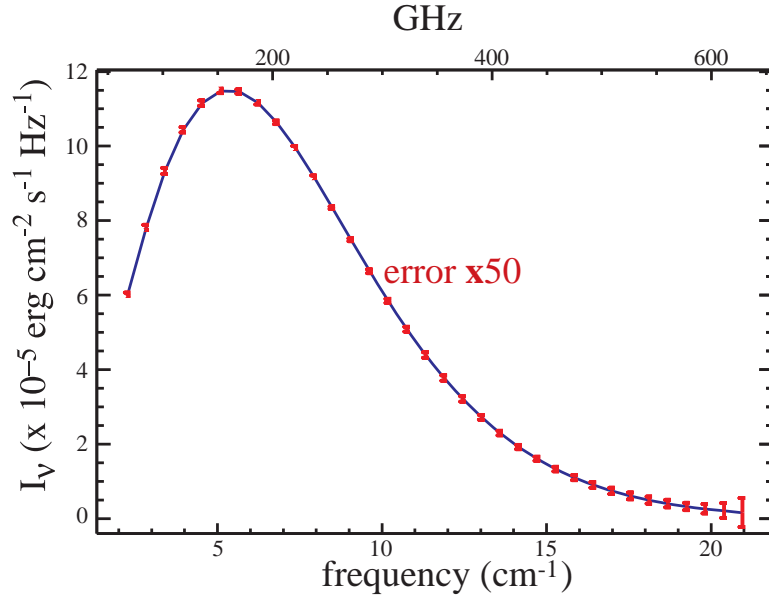


Fig. 4. CMB spectrum from FIRAS. No spectral distortions from a blackbody have been discovered to date.

to evolve until recombination which brings the low frequency spectrum back to a blackbody but now at the electron temperature.

The best limits to date are from COBE FIRAS from intermediate to high frequencies: $|\mu| < 9 \times 10^{-5}$ and $|y| < 1.5 \times 10^{-5}$ at 95% confidence (see Fig 4 and Fixsen et al. 1996). After subtracting out galactic emission, no spectral distortions of any kind are detected and the spectrum appears to be a perfect blackbody of $\bar{T} = 2.725 \pm 0.002\text{K}$ (Mather et al. 1999).

2.3 Recombination

While the recombination process



is rapid compared to the expansion, the ionization fraction obeys an equilibrium distribution just like that considered for light elements for nucleosynthesis or the CMB spectrum thermalization. As in the former two processes, the qualitative behavior of recombination is determined by the low baryon-photon ratio of the universe.

Taking number densities of the Maxwell-Boltzmann form of Eqn. (2), we obtain

$$\frac{n_p n_e}{n_H} \approx e^{-B/T} \left(\frac{m_e T}{2\pi} \right)^{3/2} e^{(\mu_p + \mu_e - \mu_H)/T}, \quad (19)$$

where $B = m_p + m_e - m_H = 13.6\text{eV}$ is the binding energy and we have set $g_p = g_e = \frac{1}{2}g_H = 2$. Given the vanishingly small chemical potential of the photons, $\mu_p + \mu_e = \mu_H$ in equilibrium.

Next, defining the ionization fraction for a hydrogen only plasma

$$\begin{aligned} n_p &= n_e = x_e n_b, \\ n_H &= n_b - n_p = (1 - x_e) n_b, \end{aligned} \quad (20)$$

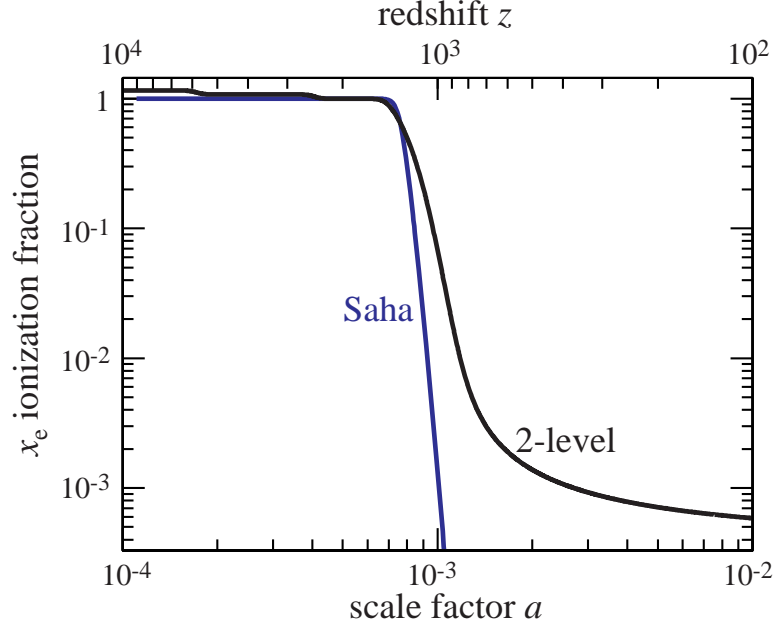


Fig. 5. Hydrogen recombination in Saha equilibrium vs. the calibrated 2-level calculation of RECFAST. The features before hydrogen recombination are due to helium recombination.

we can rewrite Eqn. (19) as the Saha equation

$$\frac{n_e n_p}{n_H n_b} = \frac{x_e^2}{1 - x_e} = \frac{1}{n_b} \left(\frac{m_e T}{2\pi} \right)^{3/2} e^{-B/T}. \quad (21)$$

Recombination occurs at a temperature substantially lower than $T = B$ again because of the low baryon-photon ratio of the universe. We can see this by rewriting the Saha equation in terms of the photon number density

$$\frac{x_e^2}{1 - x_e} = e^{-B/kT} \frac{\pi^{1/2}}{2^{5/2} \eta_{b\gamma} \zeta(3)} \left(\frac{m_e c^2}{kT} \right)^{3/2}. \quad (22)$$

Because $\eta_{b\gamma} \sim 10^{-9}$, the Saha equation implies that the medium only becomes substantially neutral at a temperature of $T \approx 0.3\text{eV}$ or at a redshift of $z_* \sim 10^3$. At this point, there are not enough photons in the even in the Wien tail above the binding energy to ionize hydrogen. We plot the Saha solution in Fig. 5.

Near the epoch of recombination, the recombination rates become insufficient to maintain ionization equilibrium. There is also a small contribution from helium recombination that must be added. The current standard for following the non-equilibrium ionization history is RECFAST (Seager et al. 2000) which employs the traditional two-level atom calculation of Peebles (1968) but alters the hydrogen case B recombination rate α_B to fit the results of a multilevel atom. More specifically, RECFAST solves a coupled system of equations for the ionization fraction x_i in singly ionized hydrogen and helium ($i = \text{H, He}$)

$$\frac{dx_i}{d \ln a} = \frac{\alpha_B C_i n_{Hp}}{H} [s(x_{\max} - x_i) - x_i x_e], \quad (23)$$

where $n_{Hp} = (1 - Y_p)n_b$ is the total hydrogen plus proton number density accounting for the helium

mass fraction Y_p , $x_e \equiv n_e/n_{Hp} = \sum x_i$ is the total ionization fraction, n_e is the free electron density, x_{\max} is the maximum x_i achieved through full ionization,

$$\begin{aligned} s &= \frac{\beta}{n_{Hp}} e^{-B_{1s}/T_b}, \\ C_i^{-1} &= 1 + \frac{\beta \alpha_B e^{-B_{2s}/T_b}}{\Lambda_\alpha + \Lambda_{2s1s}}, \\ \beta &= g_{\text{rat}} \left(\frac{T_b m_e}{2\pi} \right)^{3/2}, \end{aligned} \quad (24)$$

with g_{rat} the ratio of statistical weights, T_b the baryon temperature, B_L the binding energy of the L th level, Λ_α the rate of redshifting out of the Lyman- α line corrected for the energy difference between the $2s$ and $2p$ states

$$\Lambda_\alpha = \frac{1}{\pi^2} (B_{1s} - B_{2p})^3 e^{-(B_{2s} - B_{2p})/T_b} \frac{H}{(x_{\max} - x_i) n_{Hp}} \quad (25)$$

and Λ_{2s1s} as the rate for the 2 photon $2s - 1s$ transition. For reference, for hydrogen $B_{1s} = 13.598\text{eV}$, $B_{2s} = B_{2p} = B_{1s}/4$, $\Lambda_{2s1s} = 8.22458s^{-1}$, $g_{\text{rat}} = 1$, $x_{\max} = 1$. For helium $B_{1s} = 24.583\text{eV}$, $B_{2s} = 3.967\text{eV}$, $B_{2p} = 3.366\text{eV}$, $\Lambda_{2s1s} = 51.3s^{-1}$, $g_{\text{rat}} = 4$, $x_{\max} = Y_p/[4(1 - Y_p)]$.

Note that if the recombination rate is faster than the expansion rate $\alpha_B C_i n_{Hp}/H \gg 1$, the ionization solutions for x_i reach the Saha equilibrium $dx_i/d\ln a = 0$. In this case $s(x_{\max} - x_i) = x_i x_e$ or

$$\begin{aligned} x_i &= \frac{1}{2} \left[\sqrt{(x_{ei} + s)^2 + 4s x_{\max}} - (x_{ei} + s) \right] \\ &= x_{\max} \left[1 - \frac{x_{ei} + x_{\max}}{s} \left(1 - \frac{x_{ei} + 2x_{\max}}{s} \right) + \dots \right], \end{aligned} \quad (26)$$

where $x_{ei} = x_e - x_i$ is the ionization fraction excluding the species. The recombination of hydrogenic doubly ionized helium is here handled purely through the Saha equation with a binding energy of $1/4$ the B_{1s} of hydrogen and $x_{\max} = Y_p/[4(1 - Y_p)]$. The case B recombination coefficients as a function of T_b are given in Seager et al. (2000) as is the strong thermal coupling between T_b and T_{CMB} . The multilevel-atom fudge that RECFAST introduces is to replace the hydrogen $\alpha_B \rightarrow 1.14\alpha_B$ independently of cosmology. While this fudge suffices for current observations, which approach the $\sim 1\%$ level, the recombination standard will require improvement if CMB anisotropy predictions are to reach an accuracy of 0.1% (e.g. Switzer and Hirata 2007; Wong et al. 2007).

The phenomenology of CMB temperature and polarization anisotropy is primarily governed by the redshift of recombination $z_* = a_*^{-1} - 1$ when most of the contributions originate. This redshift though carries little dependence on standard cosmological parameters. This insensitivity follows from the fact that recombination proceeds rapidly once B_{1s}/T_b has reached a certain threshold as the Saha equation illustrates. Defining the redshift of recombination as the epoch at which the Thomson optical depth during recombination (*i.e.* excluding reionization) reaches unity, $\tau_{\text{rec}}(a_*) = 1$, a fit to the recombination calculation gives (Hu 2005)

$$a_*^{-1} \approx 1089 \left(\frac{\Omega_m h^2}{0.14} \right)^{0.0105} \left(\frac{\Omega_b h^2}{0.024} \right)^{-0.028}, \quad (27)$$

around a fiducial model of $\Omega_m h^2 = 0.14$ and $\Omega_b h^2 = 0.024$.

The universe is known to be reionized at low redshifts due to the lack of a Gunn-Peterson trough in

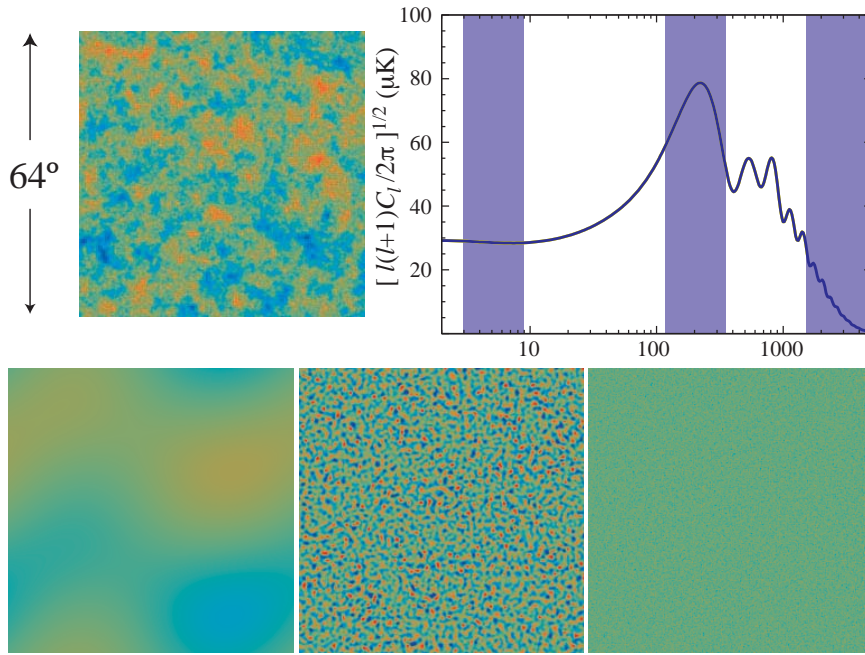


Fig. 6. From temperature maps to power spectrum. The original temperature fluctuation map (top left) corresponding to a simulation of the power spectrum (top right) can be band filtered to illustrate the power spectrum in three characteristic regimes: the large-scale gravitational regime of COBE, the first acoustic peak where most of the power lies, and the damping tail where fluctuations are dissipated. Adapted from Hu and White (2004).

quasar absorption spectra. Moreover, large angle CMB polarization detections (see Fig. 19) suggest that this transition back to full ionization occurred around $z \sim 10$ leaving an extended neutral period between recombination and reionization.

3 Temperature Anisotropy from Recombination

Spatial variations in the CMB temperature at recombination are seen as temperature anisotropy by the observer today. The temperature anisotropy of the CMB was first detected in 1992 by the COBE DMR instrument (Smoot et al. 1992). These corresponded to variations of order $\Delta T/T \sim 10^{-5}$ across $10^\circ - 90^\circ$ on the sky (see Fig. 6).

Most of the structure in the temperature anisotropy however is associated with acoustic oscillations of the photon-baryon plasma on $\sim 1^\circ$ scales. Throughout the 1990's constraints on the location of the first peak steadily improved culminating with the determinations of the TOCO (Miller et al. 1999), Boomerang, (de Bernardis et al. 2000) and Maxima-1 (Hanany et al. 2000) experiments. Currently from WMAP (Spergel et al. 2007) and ground based experiments, we have precise measurements of the first five acoustic peaks (see Fig. 7). Primary fluctuations beyond this scale (below $\sim 10'$) are damped by Silk damping (Silk 1968) as verified observationally first by the CBI experiment (Padin et al. 2001).

In this section, we deconstruct the basic physics behind these phenomena. We begin with the geometric projection of temperature inhomogeneities at recombination onto the sky of the observer in §3.1. We continue with the basic equations of fluid mechanics that govern acoustic phenomena in §3.2. We add gravitational (§3.3), baryonic (§3.4), matter-radiation (§3.5), and dissipational (§3.6)

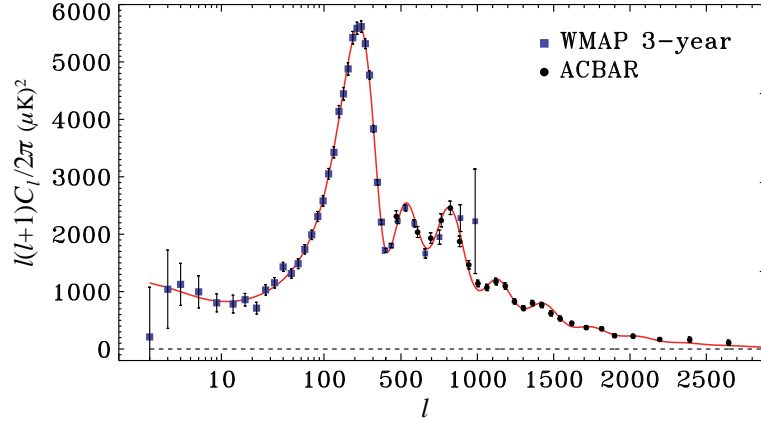


Fig. 7. Temperature power spectrum from recent measurements from WMAP and ACBAR along with the best fit Λ CDM model. The main features of the temperature power spectrum including the first 5 acoustic peaks and damping tail have now been measured. Adapted from Reichardt et al. (2008).

effects in the sections that follow. Finally we put these pieces back together to discuss the information content of the acoustic peaks in §3.7.

3.1 Anisotropy from Inhomogeneity

Given that the CMB radiation is blackbody to experimental accuracy (see Fig. 4), one can characterize its spatial and angular distribution by its temperature at the position \mathbf{x} of the observer in the direction $\hat{\mathbf{n}}$ on the observer's sky

$$f(\nu, \hat{\mathbf{n}}, \mathbf{x}) = [\exp(2\pi\nu/T(\hat{\mathbf{n}}; \mathbf{x}) - 1)]^{-1}, \quad (28)$$

where $\nu = E/2\pi$ is the observation frequency. The hypothetical observer could be an electron in the intergalactic medium or the true observer on earth or L2. When the latter is implicitly meant, we will take $\mathbf{x} = \mathbf{0}$. We will occasionally suppress the coordinate \mathbf{x} when this position is to be understood.

For statistically isotropic, Gaussian random temperature fluctuations a harmonic description is more efficient than a real space description. For the angular structure at the position of the observer, the appropriate harmonics are the spherical harmonics. These are the eigenfunctions of the Laplace operator on the sphere and form a complete basis for scalar functions on the sky

$$\Theta(\hat{\mathbf{n}}) = \frac{T(\hat{\mathbf{n}}) - \bar{T}}{\bar{T}} = \sum_{\ell m} \Theta_{\ell m} Y_{\ell m}(\hat{\mathbf{n}}). \quad (29)$$

For statistically isotropic fluctuations, the ensemble average of the temperature fluctuations are described by the power spectrum

$$\langle \Theta_{\ell m}^* \Theta_{\ell' m'} \rangle = \delta_{\ell\ell'} \delta_{mm'} C_\ell. \quad (30)$$

Moreover, the power spectrum contains all of the statistical information in the field if the fluctuations are Gaussian. Here C_ℓ is dimensionless but is often shown with units of squared temperature, *e.g.* μK^2 , by multiplying through by the background temperature today \bar{T} . The correspondence between angular size and amplitude of fluctuations and the power spectrum is shown in Fig. 6.

Let us begin with the simple approximation that the temperature field at recombination is isotropic

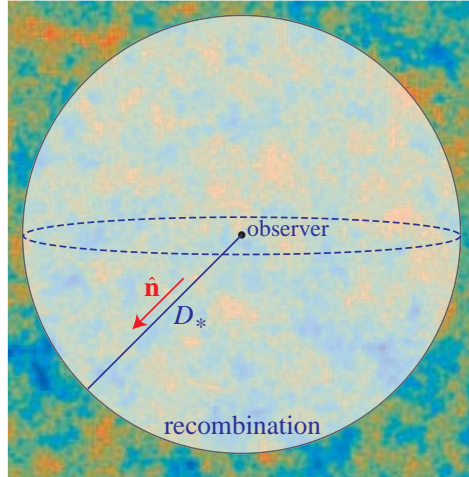


Fig. 8. From inhomogeneity to anisotropy. Temperature inhomogeneities at recombination are viewed at a distance D_* as anisotropy on the observer's sky.

but inhomogeneous and the anisotropy viewed at the present is due to the observer seeing different portions of the recombination surface in different directions (see Fig. 8). We will develop this picture further in the following sections with gravitational redshifts, dipole or Doppler anisotropic sources, the finite duration of recombination, and polarization.

Under this simple instantaneous recombination approximation, the angular temperature fluctuation distribution is simply a projection of the spatial temperature fluctuation

$$\Theta(\hat{\mathbf{n}}) = \int dD \Theta(\mathbf{x}) \delta(D - D_*), \quad (31)$$

where $D = \int dz/H$ is the comoving distance and D_* denotes the distance a CMB photon travels from recombination. Here $\Theta(\mathbf{x}) = (T(\mathbf{x}) - \bar{T})/\bar{T}$ is the spatial temperature fluctuation at recombination. Note that the cosmological redshift does not appear in the temperature fluctuation since the background and fluctuation redshift alike.

The spatial power spectrum at recombination can be likewise be described by its harmonic modes. In a flat geometry, these are Fourier modes

$$\Theta(\mathbf{x}) = \int \frac{d^3k}{(2\pi)^3} \Theta(\mathbf{k}) e^{i\mathbf{k}\cdot\mathbf{x}}. \quad (32)$$

More generally they are the eigenfunctions of the Laplace operator on the three dimensional space with constant curvature of a general Friedmann-Robertson-Walker metric (see *e.g.* Hu 2003). For a statistically homogeneous spatial distribution, the two point function is described by the power spectrum

$$\langle \Theta(\mathbf{k})^* \Theta(\mathbf{k}') \rangle = (2\pi)^3 \delta(\mathbf{k} - \mathbf{k}') P(k). \quad (33)$$

These relations tell us that the amplitude of the angular and spatial power spectra are related. A useful way of establishing this relation and quantifying the power in general is to describe the contribution per logarithmic interval to the variance of the respective fields:

$$\langle \Theta(\mathbf{x}) \Theta(\mathbf{x}) \rangle = \int \frac{d^3k}{(2\pi)^3} P(k) = \int d \ln k \frac{k^3 P(k)}{2\pi^2} \equiv \int d \ln k \Delta_T^2(k). \quad (34)$$

A scale invariant spectrum has equal contribution to the variance per e-fold $\Delta_T^2 = k^3 P(k)/2\pi^2 = \text{const.}$ To relate this to the amplitude of the angular power spectrum, we expand equation (31) in Fourier modes

$$\Theta(\hat{\mathbf{n}}) = \int \frac{d^3k}{(2\pi)^3} \Theta(\mathbf{k}) e^{i\mathbf{k} \cdot D_* \hat{\mathbf{n}}}. \quad (35)$$

The Fourier modes themselves can be expanded in spherical harmonics with the relation

$$e^{i\mathbf{k} \cdot D_* \hat{\mathbf{n}}} = 4\pi \sum_{\ell m} i^\ell j_\ell(kD_*) Y_{\ell m}^*(\hat{\mathbf{k}}) Y_{\ell m}(\hat{\mathbf{n}}), \quad (36)$$

where j_ℓ is the spherical Bessel function. Extracting the multipole moments, we obtain

$$\Theta_{\ell m} = \int \frac{d^3k}{(2\pi)^3} \Theta(\mathbf{k}) 4\pi i^\ell j_\ell(kD_*) Y_{\ell m}(\mathbf{k}). \quad (37)$$

We can then relate the angular and spatial two point functions (30) and (33)

$$\langle \Theta_{\ell m}^* \Theta_{\ell' m'} \rangle = \delta_{\ell\ell'} \delta_{mm'} 4\pi \int d \ln k j_\ell^2(kD_*) \Delta_T^2(k) = \delta_{\ell\ell'} \delta_{mm'} C_\ell. \quad (38)$$

Given a slowly varying, nearly scale invariant spatial power spectrum we can take Δ_T^2 out of the integral and evaluate it at the peak of the Bessel function $kD_* \approx \ell$. The remaining integral can be evaluated in closed form $\int_0^\infty j_\ell^2(x) d \ln x = 1/[2\ell(\ell+1)]$ yielding the final result

$$C_\ell \approx \frac{2\pi}{\ell(\ell+1)} \Delta_T^2(\ell/D_*). \quad (39)$$

Likewise even slowly varying features like the acoustic peaks of §3.2 also mainly map to multipoles of $\ell \approx kD_*$ due to the delta function like behavior of j_ℓ^2 .

It is therefore common to plot the angular power spectrum as

$$\mathcal{C}_\ell \equiv \frac{\ell(\ell+1)}{2\pi} C_\ell \approx \Delta_T^2. \quad (40)$$

It is also common to plot $\mathcal{C}_\ell^{1/2} \approx \Delta_T$, the logarithmic contribution to the rms of the field, in units of μK .

Now let us compare this expression to the variance per log interval in multipole space:

$$\begin{aligned} \langle T(\hat{\mathbf{n}}) T(\hat{\mathbf{n}}) \rangle &= \sum_{\ell m} \sum_{\ell' m'} \langle T_{\ell m}^* T_{\ell' m'} \rangle Y_{\ell m}^*(\hat{\mathbf{n}}) Y_{\ell' m'}(\hat{\mathbf{n}}) \\ &= \sum_{\ell} C_\ell \sum_m Y_{\ell m}^*(\hat{\mathbf{n}}) Y_{\ell m}(\hat{\mathbf{n}}) = \sum_{\ell} \frac{2\ell+1}{4\pi} C_\ell. \end{aligned} \quad (41)$$

For variance contributions from $\ell \gg 1$,

$$\sum_{\ell} \frac{2\ell+1}{4\pi} C_\ell \approx \int d \ln \ell \ell \frac{\ell(2\ell+1)}{4\pi} C_\ell \approx \int d \ln \ell \frac{\ell(\ell+1)}{2\pi} C_\ell. \quad (42)$$

Thus \mathcal{C}_ℓ is also approximately the variance per log interval in angular space as well.

3.2 Acoustic Oscillation Basics

Thomson Tight Coupling — To understand the angular pattern of temperature fluctuations seen by the observer today, we must understand the spatial temperature pattern at recombination. That in turn requires an understanding of the dominant physical processes in the plasma before recombination.

Thomson scattering of photons off of free electrons is the most important process given its relatively large cross section (averaged over polarization states)

$$\sigma_T = \frac{8\pi\alpha^2}{3m_e^2} = 6.65 \times 10^{-25} \text{cm}^2. \quad (43)$$

The important quantity to consider is the mean free path of a photon given Thomson scattering and a medium with a free electron density n_e . Before recombination when the ionization fraction $x_e \approx 1$ this density is given by

$$\begin{aligned} n_e &= (1 - Y_p)x_e n_b \\ &= 1.12 \times 10^{-5} (1 - Y_p)x_e \Omega_b h^2 (1 + z)^3 \text{cm}^{-3}. \end{aligned} \quad (44)$$

The comoving mean free path λ_C is given by

$$\lambda_C^{-1} \equiv \dot{\tau} \equiv n_e \sigma_T a, \quad (45)$$

where the extra factor of a comes from converting physical to comoving coordinates and Y_p is the primordial helium mass fraction. We have also represented this mean free path in terms of an scattering absorption coefficient $\dot{\tau}$ where dots are conformal time $\eta \equiv \int dt/a$ derivatives and τ is the optical depth.

Near recombination ($z \approx 10^3$, $x_e \approx 1$) and given $\Omega_b h^2 \approx 0.02$, and $Y_p = 0.24$, the mean free path is

$$\lambda_C \equiv \frac{1}{\dot{\tau}} \sim 2.5 \text{Mpc}. \quad (46)$$

This scale is almost two orders of magnitude smaller than the horizon at recombination. On scales $\lambda \gg \lambda_C$ photons are tightly coupled to the electrons by Thomson scattering which in turn are tightly coupled to the baryons by Coulomb interactions.

As a consequence, any bulk motion of the photons must be shared by the baryons. In fluid language, the two species have a single bulk velocity $v_\gamma = v_b$ and hence no entropy generation or heat conduction occurs. Furthermore, the shear viscosity of the fluid is negligible. Shear viscosity is related to anisotropy in the radiative pressure or stress and rapid scattering isotropizes the photon distribution. This is also the reason why in equation (31) we took the photon distribution to be isotropic but inhomogeneous.

We shall see that the fluid motion corrects this by allowing dipole $\ell = 1$ anisotropy in the distribution but no higher ℓ modes. It is only on scales smaller than the diffusion scale that radiative viscosity ($\ell = 2$) and heat conduction becomes sufficiently large to dissipates the bulk motions of the plasma (see §3.6).

Zeroth Order Approximation — To understand the basic physical picture, let us begin our discussion of acoustic oscillations in the tight coupling regime with a simplified system which we will refine as we progress.

First let us ignore the dynamical impact of the baryons on the fluid motion. Given that the baryon and photon velocity are equal and the momentum density of a relativistic fluid is given by $(\rho + p)v$,

where p is the pressure, and v is the fluid velocity, this approximation relates to the quantity

$$\begin{aligned} R &\equiv \frac{(\rho_b + p_b)v_b}{(\rho_\gamma + p_\gamma)v_\gamma} = \frac{\rho_b + p_b}{\rho_\gamma + p_\gamma} = \frac{3\rho_b}{4\rho_\gamma} \\ &\approx 0.6 \left(\frac{\Omega_b h^2}{0.02} \right) \left(\frac{a}{10^{-3}} \right), \end{aligned} \quad (47)$$

where we have used the fact that $\rho_\gamma \propto T^4$ so that its value is fixed by the redshifting background $\bar{T} = 2.725(1+z)\text{K}$. Neglect of the baryon inertia and momentum only fails right around recombination.

Next, we shall assume that the background expansion is matter dominated to relate time and scale factor. The validity of this approximation depends on the matter-radiation ratio

$$\frac{\rho_m}{\rho_r} = 3.6 \left(\frac{\Omega_m h^2}{0.15} \right) \left(\frac{a}{10^{-3}} \right), \quad (48)$$

and is approximately valid during recombination and afterwards. One expects from these arguments that order unit differences between the real universe and our basic description will occur. We will in fact use these differences in the following sections to show how the baryon and matter densities are measured from the acoustic peak morphology.

Finally, we shall consider the effect of pressure forces and neglect gravitational forces. While this is not a valid approximation in and of itself, we shall see that for a photon-dominated system, the error in ignoring gravitational forces exactly cancels with that from ignoring gravitational redshifts that photons experience after recombination (see §3.3).

Continuity Equation — Given that Thomson scattering neither creates nor destroys photons, the continuity equation implies that the photon number density only changes due to flows into and out of the volume. In a non expanding universe that would require

$$\dot{n}_\gamma + \nabla \cdot (n_\gamma \mathbf{v}_\gamma) = 0. \quad (49)$$

Since n_γ is the number density of photons per unit physical (not comoving) volume, this equation must be corrected for the expansion. The effect of the expansion can alternately be viewed as that of the Hubble flow diluting the number density everywhere in space. Because number densities scale as $n_\gamma \propto a^{-3}$, the expansion alters the continuity equation as

$$\dot{n}_\gamma + 3n_\gamma \frac{\dot{a}}{a} + \nabla \cdot (n_\gamma \mathbf{v}_\gamma) = 0. \quad (50)$$

Since we are interested in small fluctuations around the background, let us linearize the equations $n_\gamma \approx \bar{n}_\gamma + \delta n_\gamma$ and drop terms that are higher than first order in $\delta n_\gamma / n_\gamma$ and v_γ . Note that v_γ is first order in the number density fluctuations since as we shall see in the Euler equation discussion below it is generated from the pressure gradients associated with density fluctuations.

The continuity equation (50) for the fluctuations becomes

$$\left(\frac{\delta n_\gamma}{n_\gamma} \right)' = -\nabla \cdot \mathbf{v}_\gamma. \quad (51)$$

Since the number density $n_\gamma \propto T^3$, the fractional density fluctuation is related to the temperature fluctuation Θ as

$$\frac{\delta n_\gamma}{n_\gamma} = 3 \frac{\delta T}{T} \equiv 3\Theta. \quad (52)$$

Expressing the continuity equation in terms of Θ , we obtain

$$\dot{\Theta} = -\frac{1}{3}\nabla \cdot \mathbf{v}_\gamma. \quad (53)$$

Fourier transforming this equation, we get

$$\dot{\Theta} = -\frac{1}{3}i\mathbf{k} \cdot \mathbf{v}_\gamma, \quad (54)$$

for the relationship between the Fourier mode amplitudes.

Euler Equation — Now let us examine the origin of the fluid velocity. In the background, the velocity vanishes due to isotropy. However, Newtonian mechanics dictates that pressure forces will generate particle momentum as $\dot{\mathbf{q}} = \mathbf{F}$. Newton's law must also be modified for the expansion. If we associate the de Broglie wavelength with the inverse momentum, this wavelength also stretches with the expansion. For photons, this accounts for the redshift factor. For non-relativistic matter, this means that bulk velocities decay with the expansion. In either case, we generalize Newton's law to read

$$\dot{\mathbf{q}} + \frac{\dot{a}}{a}\mathbf{q} = \mathbf{F}. \quad (55)$$

For a collection of particles, the relevant quantity is the momentum density

$$(\rho_\gamma + p_\gamma)\mathbf{v}_\gamma \equiv \int \frac{d^3q}{(2\pi)^3} \mathbf{q} f, \quad (56)$$

and likewise the force becomes a force density. For the photon-baryon fluid, this force density is provided by the pressure gradient. The result is the Euler equation

$$[(\rho_\gamma + p_\gamma)\mathbf{v}_\gamma]' = -4\frac{\dot{a}}{a}(\rho_\gamma + p_\gamma)\mathbf{v}_\gamma - \nabla p_\gamma, \quad (57)$$

where the 4 on the right hand side comes from combining the redshifting of wavelengths with that of number densities. Since photons have an equation of state $p_\gamma = \rho_\gamma/3$, the Euler equation becomes

$$\begin{aligned} \frac{4}{3}\rho_\gamma \dot{\mathbf{v}}_\gamma &= -\frac{1}{3}\nabla p_\gamma, \\ \dot{\mathbf{v}}_\gamma &= -\nabla\Theta. \end{aligned} \quad (58)$$

In Fourier space, the Euler equation becomes

$$\dot{\mathbf{v}}_\gamma = -i\mathbf{k}\Theta. \quad (59)$$

The factor of i here represents the fact that the temperature maxima and minima are zeros of the velocity in real space due to the gradient relation, *i.e.* temperature and velocity have a $\pi/2$ phase shift. It is convenient therefore to define the velocity amplitude to absorb this factor

$$\mathbf{v}_\gamma \equiv -iv_\gamma \hat{\mathbf{k}}. \quad (60)$$

The direction of the fluid velocity is always parallel to the wavevector \mathbf{k} for linear (scalar) perturbations and hence we can write the Euler equation as

$$\dot{v}_\gamma = k\Theta. \quad (61)$$

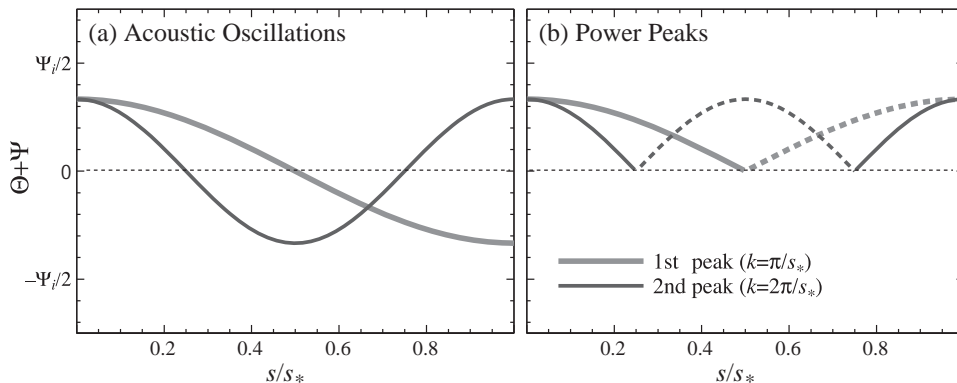


Fig. 9. Acoustic oscillation basics. All modes start from the same initial epoch with time denoted by the sound horizon relative to the sound horizon at recombination s_* . (a) Wavenumbers that reach extrema in their effective temperature $\Theta + \Psi$ (accounting for gravitational redshifts §3.3) at s_* form a harmonic series $k_n = n\pi/s_*$. (b) Amplitude of the fluctuations is the same for the maxima and minima without baryon inertia. Adapted from Hu and Dodelson (2002).

Acoustic Peaks — Combining the continuity (54) and Euler (61) equations to eliminate the fluid velocity, we get the simple harmonic oscillator equation

$$\ddot{\Theta} + c_s^2 k^2 \Theta = 0, \quad (62)$$

where the adiabatic sound speed $c_s^2 = 1/3$ for the photon-dominated fluid and more generally is defined as

$$c_s^2 \equiv \frac{\dot{p}_\gamma}{\dot{\rho}_\gamma}. \quad (63)$$

The solution to the oscillator equation can be specified given two initial conditions $\Theta(0)$ and $v_\gamma(0)$ or $\dot{\Theta}(0)$,

$$\Theta(\eta) = \Theta(0) \cos(ks) + \frac{\dot{\Theta}(0)}{kc_s} \sin(ks), \quad (64)$$

where the sound horizon is defined as

$$s \equiv \int c_s d\eta. \quad (65)$$

In real space, these oscillations appear as standing waves for each Fourier mode.

These standing waves continue to oscillate until recombination. At this point the free electron density drops drastically (see Fig. 5) and the photons freely stream to the observer. The pattern of acoustic oscillations on the recombination surface seen by the observer becomes the acoustic peaks in the temperature anisotropy.

Let us focus on the adiabatic mode which starts with a finite density or temperature fluctuation and vanishing velocity perturbation. At recombination η_* , the oscillation reaches (see Fig. 9)

$$\Theta(\eta_*) = \Theta(0) \cos(ks_*). \quad (66)$$

Considering a spectrum of k modes, the critical feature of these oscillations are that they are temporally coherent. The underlying assumption is that fluctuations of all wavelengths originated at $\eta = 0$ or at least $\eta \ll \eta_*$. Without inflation this would violate causality for long wavelength fluctuations, *i.e.*

the analogue of the horizon problem for perturbations. With inflation, superhorizon modes originate during an inflationary epoch $\eta_i \ll \eta_*$.

Modes caught in the extrema of their oscillation follow a harmonic relation

$$k_n s_* = n\pi, \quad n = 1, 2, 3 \dots \quad (67)$$

yielding a fundamental scale or frequency, related to the inverse sound horizon

$$k_A = \pi/s_*. \quad (68)$$

Since the power spectrum is proportional to the square of the fluctuation, both maxima and minima contribute peaks in the spectrum. Observational verification of this harmonic series is the primary evidence for inflationary adiabatic initial conditions (Hu and White 1996).

The fundamental physical scale is translated into a fundamental angular scale by simple projection according to the angular diameter distance D_A

$$\begin{aligned} \theta_A &= \lambda_A/D_A, \\ \ell_A &= k_A D_A, \end{aligned} \quad (69)$$

(see Eqn. (39)). In a flat universe, the distance is simply $D_A = D \equiv \eta_0 - \eta_* \approx \eta_0$, the horizon distance, and $k_A = \pi/s_* = \sqrt{3}\pi/\eta_*$ so

$$\theta_A \approx \frac{\eta_*}{\eta_0}. \quad (70)$$

Furthermore, in a matter-dominated universe $\eta \propto a^{1/2}$ so $\theta_A \approx 1/30 \approx 2^\circ$ or

$$\ell_A \approx 200. \quad (71)$$

We shall see in §3.7 that radiation and dark energy introduce important corrections to this prediction from their influence on η_* and D_* respectively. Nonetheless it is remarkable that this simple argument predicts the basics of acoustic oscillations: their existence, coherence and fundamental scale.

Acoustic Troughs: Doppler Effect — Acoustic oscillations also imply that the plasma is moving relative to the observer. This bulk motion imprints a temperature anisotropy via the Doppler effect

$$\left(\frac{\Delta T}{T}\right)_{\text{dop}} = \hat{\mathbf{n}} \cdot \mathbf{v}_\gamma. \quad (72)$$

Averaged over directions

$$\left(\frac{\Delta T}{T}\right)_{\text{rms}} = \frac{v_\gamma}{\sqrt{3}}, \quad (73)$$

which given the acoustic solution of Eqn. (64) implies

$$\begin{aligned} \frac{v_\gamma}{\sqrt{3}} &= -\frac{\sqrt{3}}{k} \dot{\Theta} = \frac{\sqrt{3}}{k} k c_s \Theta(0) \sin(ks) \\ &= \Theta(0) \sin(ks). \end{aligned} \quad (74)$$

Interestingly, the Doppler effect for the photon-dominated system is of equal amplitude and $\pi/2$ out of phase: extrema of temperature are turning points of velocity. If we simply add the k -space temperature and Doppler effects in quadrature we would obtain

$$\left(\frac{\Delta T}{T}\right)^2 = \Theta^2(0) [\cos^2(ks) + \sin^2(ks)] = \Theta^2(0). \quad (75)$$

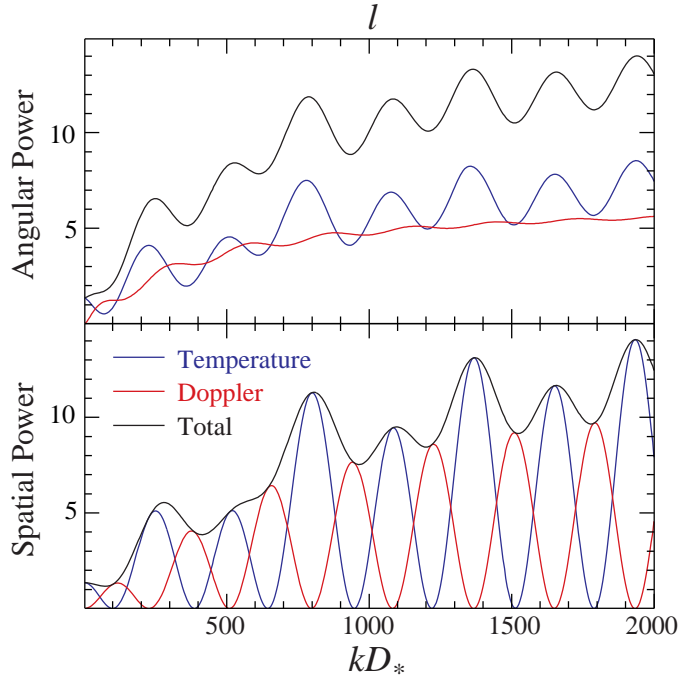


Fig. 10. Doppler effect. The Doppler effect provides fluctuations of comparable strength to the local temperature fluctuations from acoustic oscillations in k -space (lower) providing features at the troughs of the latter. In angular space, projection effects smooth the Doppler features leaving an acoustic morphology that reflects the temperature oscillations. The peak height modulation comes from the baryon inertia (§3.4) and the gradual increase in power with ℓ from radiation domination (§3.5).

In other words there are no preferred k -modes at harmonics and a scale invariant initial temperature spectrum would lead to a scale invariant spatial power spectrum at recombination. However the Doppler effect carries an angular dependence that changes its projection on the sky $\hat{\mathbf{n}} \cdot \mathbf{v}_\gamma \propto \hat{\mathbf{n}} \cdot \hat{\mathbf{k}}$. In a coordinate system where $\hat{\mathbf{z}} \parallel \hat{\mathbf{k}}$, this angular dependence yields an extra factor of Y_{10} in the analogue of Eqn. (38). This extra factor can be reabsorbed into the total angular dependence through Clebsch-Gordan recoupling (Hu and White 1997)

$$Y_{10}Y_{\ell 0} \rightarrow Y_{\ell \pm 10}. \quad (76)$$

The recoupling implied for the radial harmonics changes $j_\ell(x) \rightarrow j'_\ell(x)$. The projection kernel $j'_\ell(x)$ lacks a strong feature at $\ell \sim x$ and so Doppler contributions in k are spread out in ℓ . This is simply a mathematical way of stating that the Doppler effect vanishes when the observer is looking perpendicular to $\mathbf{v} \parallel \mathbf{k}$ whereas it is in that direction that the acoustic peaks in temperature gain most of their contribution. The net effect, including baryonic effects that we discuss below, is that the peak structure is dominated by the local temperature at recombination and not the local fluid motion.

3.3 Gravito-Acoustic Oscillations

Thus far we have neglected gravitational forces and redshifts in our discussion of plasma motion. The true system exhibits gravito-acoustic or Jeans oscillations. We were able to employ this swindle to

get the basic properties of acoustic oscillations because in a photon-dominated plasma the effect of gravitational forces and gravitational redshifts exactly cancel in constant gravitational potentials. To go beyond the photon dominated plasma and matter dominated expansion approximation, we now need to include these effects. Furthermore, we shall see that the gravitational potential perturbations from inflation are also the source of the initial temperature fluctuation.

Continuity Equation and Newtonian Curvature — The photon continuity equation for the number density is altered by gravity since the presence of a gravitational potential alters the coordinate volume. Formally in general relativity this comes from the space-space piece of the metric – a spatial curvature perturbation Φ :

$$ds^2 = a^2[-(1 + 2\Psi)d\eta^2 + (1 + 2\Phi)dx^2] \quad (77)$$

for a flat cosmology.

We can think of this curvature perturbation as changing the local scale factor $a \rightarrow a(1 + \Phi)$ so that the expansion dilution is generalized to

$$\frac{\dot{a}}{a} \rightarrow \frac{\dot{a}}{a} + \dot{\Phi}. \quad (78)$$

Hence the full continuity equation is now given by

$$(\delta n_\gamma)' = -3\delta n_\gamma \frac{\dot{a}}{a} - 3n_\gamma \dot{\Phi} - n_\gamma \nabla \cdot \mathbf{v}_\gamma, \quad (79)$$

or

$$\dot{\Theta} = -\frac{1}{3}kv_\gamma - \dot{\Phi}. \quad (80)$$

Euler Equation and Newtonian Forces — Likewise the gravitational force from gradients in the gravitational potential (Ψ , formally the time-time piece of the metric perturbation) modifies the momentum conservation equation. The Newtonian force $\mathbf{F} = -m\nabla\Psi$ generalized to momentum density brings the Euler equation to

$$\dot{v}_\gamma = k(\Theta + \Psi). \quad (81)$$

General relativity says that Φ and Ψ are the relativistic analogues of the Newtonian potential and that $\Phi \approx -\Psi$ in the absence of sources of anisotropic stress or viscosity.

Photon Dominated Oscillator — We can again combine the continuity equation (80) and Euler equation (81) to form the forced simple harmonic oscillator system

$$\ddot{\Theta} + c_s^2 k^2 \Theta = -\frac{k^2}{3}\Psi - \ddot{\Phi}. \quad (82)$$

Note that the effect of baryon inertia is still absent in this system. To make further progress in understanding the effect of gravity on acoustic oscillations we need to specify the gravitational potential $\Psi \approx -\Phi$ from the Poisson equation and understand its time evolution.

Poisson Equation and Constant Potentials — In our matter-dominated approximation, Φ is generated by matter density fluctuations Δ_m through the cosmological Poisson equation

$$k^2\Phi = 4\pi G a^2 \rho_m \Delta_m, \quad (83)$$

where the difference from the usual Poisson equation comes from the use of comoving coordinates

for k (a^2 factor), the removal of the background density into the background expansion ($\rho_m \Delta_m$) and finally a coordinate subtlety that enters into the definition of Δ_m . In general, the relativistic Poisson equation would have contributions from the momentum density. Alternately we can relate

$$\Delta_m = \frac{\delta \rho_m}{\rho_m} + 3 \frac{\dot{a}}{a} \frac{v_m}{k} \quad (84)$$

to the density fluctuation in a coordinate system that comoves with the matter (formally through a gauge transformation). Beyond the matter dominated approximation, the Poisson equation would carry contributions from all of the species of energy density and the comoving coordinate system would also reflect the total.

In a matter-dominated epoch (or in fact any epoch when gravitational potential gradients and not stress gradients dominate the momentum equation), the matter Euler equation implies $v_m \sim k\eta\Psi$. The matter continuity equation then implies $\Delta_m \sim -k\eta v_m \sim -(k\eta)^2\Psi$. The Poisson equation then yields $\Phi \sim \Delta_m/(k\eta)^2 \sim -\Psi$. Here we have used the Friedmann equation $H^2 = 8\pi G\rho_m/3$ and $\eta = \int d\ln a/(aH) \sim 1/(aH)$. In other words, the density perturbation Δ_m grows at exactly the right rate to keep the gravitational potential constant. More formally, if stress perturbations are negligible compared with density perturbations ($\delta p \ll \delta\rho$) then the potential will remain constant in periods where the background equation of state p/ρ is constant. With a varying equation of state, it is the comoving curvature ζ rather than the Newtonian curvature that is strictly constant (Bardeen 1980).

Effective Temperature — If the gravitational potential is constant, we can rewrite the oscillator equation (82) as

$$\ddot{\Theta} + \ddot{\Psi} + c_s^2 k^2 (\Theta + \Psi) = 0. \quad (85)$$

The solution in Eqn. (64) for adiabatic initial conditions then generalizes to

$$[\Theta + \Psi](\eta) = [\Theta + \Psi](0) \cos(ks). \quad (86)$$

Like a mass on spring in a constant gravitational field of the earth, the solution just represents oscillations around a displaced minimum.

Furthermore, $\Theta + \Psi$ is also the observed temperature fluctuation. Photons lose energy climbing out of gravitational potentials at recombination and so the observer at the present will see

$$\frac{\Delta T}{T} = \Theta + \Psi. \quad (87)$$

Therefore from the perspective of the observer, the acoustic oscillations ignoring both gravitational forces and gravitational redshifts is unchanged: initial perturbations in the effective temperature oscillate around zero with a frequency given by the sound speed. What the consideration of gravity adds is a way of connecting the initial conditions to inflationary curvature fluctuations.

The Sachs-Wolfe 1/3 — The effective temperature perturbation includes both the local temperature Θ in Newtonian coordinates and the gravitational redshift factor Ψ . For $ks_* \ll 1$, the oscillator is frozen at its initial conditions and the total is called the Sachs and Wolfe (1967) effect. The division into two pieces is actually an artifact of the coordinate system. Both pieces are determined by the initial curvature perturbation from inflation.

To see this, let us relate both the Newtonian potential and local temperature fluctuation to a change in time coordinate from comoving coordinates to Newtonian coordinates (formally through

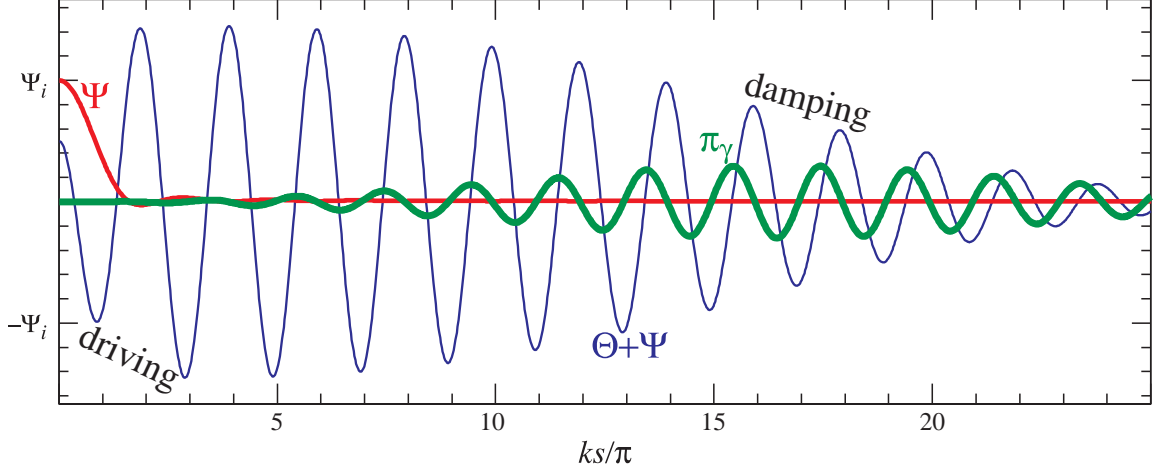


Fig. 11. Acoustic oscillations with gravitational forcing and dissipational damping. For a mode that enters the sound horizon during radiation domination, the gravitational potential decays at horizon crossing and drives the acoustic amplitude higher. As the photon diffusion length increases and becomes comparable to the wavelength, radiative viscosity π_γ is generated from quadrupole anisotropy leading to dissipation and polarization (see §4.4). Adapted from Hu and Dodelson (2002).

a gauge transformation, see White and Hu 1997 for a more detailed treatment). The Newtonian gravitational potential Ψ is a perturbation to the temporal coordinate (see Eqn. (77))

$$\frac{\delta t}{t} = \Psi. \quad (88)$$

Given the Friedmann equation, this is equivalent to a perturbation in the scale factor

$$t = \int \frac{da}{aH} \propto \int \frac{da}{a\rho^{1/2}} \propto a^{3(1+w)/2}, \quad (89)$$

where $w \equiv p/\rho$. During matter domination $w = 0$ and

$$\frac{\delta a}{a} = \frac{2}{3} \frac{\delta t}{t}. \quad (90)$$

Since the CMB temperature is cooling as $T \propto a^{-1}$ a local change in the scale factor changes the local temperature

$$\Theta = -\frac{\delta a}{a} = -\frac{2}{3}\Psi. \quad (91)$$

Combining this with Ψ to form the effective temperature gives

$$\Theta + \Psi = \frac{1}{3}\Psi. \quad (92)$$

The consequence is that overdense regions where Ψ is negative (potential wells) are cold spots in the effective temperature.

Inflation provides a source for initial curvature fluctuations. Specifically the comoving curvature perturbation ζ becomes a Newtonian curvature of

$$\Phi = \frac{3}{5}\zeta \quad (93)$$

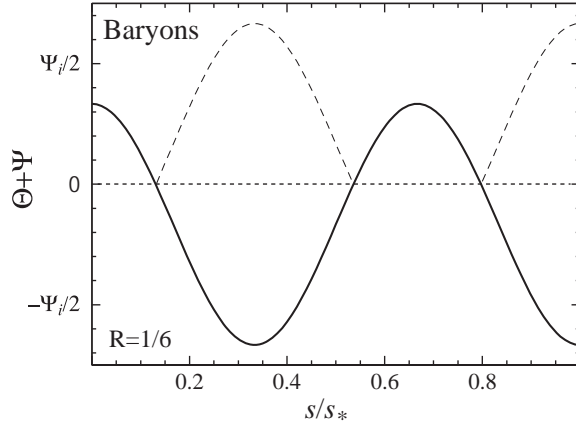


Fig. 12. Acoustic oscillations with baryons. Baryons add inertia to the photon-baryon plasma displacing the zero point of the oscillation and making compressional peaks (minima) larger than rarefaction peaks (maxima). The absolute value of the fluctuation in effective temperature is shown in dotted lines. Adapted from Hu and Dodelson (2002).

in the matter-dominated epoch. The initial amplitude of scalar curvature perturbations is usually given as $A_S = \delta_\zeta^2$ which characterizes the variance contribution per e-fold to the curvature near some fiducial wavenumber k_n (see Eqn. 34)

$$\Delta_\zeta^2 = \frac{k^3 P_\zeta}{2\pi^2} = \delta_\zeta^2 \left(\frac{k}{k_n} \right)^{n-1}, \quad (94)$$

where $n = 1$ for a scale invariant spectrum. Combining these relations for $n = 1$

$$\frac{\ell(\ell+1)C_\ell}{2\pi} \approx \frac{\delta_\zeta^2}{25}. \quad (95)$$

in the Sachs-Wolfe limit. The 10^{-5} fluctuations measured by COBE then correspond to $\delta_\zeta \approx 5 \times 10^{-5}$.

3.4 Baryonic Effects

The next level of detail that we need to add is the inertial effect of baryons in the plasma. Since equation (47) says that the baryon momentum becomes comparable to the photon momentum near recombination, we can expect order unity corrections on the basic acoustic oscillation picture from baryons. With the precise measurements of the first and second peak, this change in the acoustic morphology has already provided the most sensitive measure of the baryon-photon ratio to date exceeding that of big bang nucleosynthesis.

Baryon Loading — Baryons add extra mass to the photon-baryon plasma or equivalently an enhancement of the momentum density of the plasma given by $R = (p_b + \rho_b)/(p_\gamma + \rho_\gamma)$. Specifically the momentum density of the joint system

$$(\rho_\gamma + p_\gamma)v_\gamma + (\rho_b + p_b)v_b \equiv (1 + R)(\rho_\gamma + p_\gamma)v_{\gamma b} \quad (96)$$

is conserved. For generality, we have introduced the baryon velocity v_b and the momentum-weighted velocity $v_{\gamma b}$ but in the tightly coupled plasma $v_b \approx v_{\gamma b} \approx v_\gamma$ (*c.f.* §3.6).

The Euler equation (81) becomes

$$\begin{aligned}
 [(1+R)(\rho_\gamma + p_\gamma)\mathbf{v}_{\gamma b}]' &= -4\frac{\dot{a}}{a}(1+R)(\rho_\gamma + p_\gamma)\mathbf{v}_{\gamma b} \\
 &\quad -\nabla p_\gamma - (1+R)(\rho_\gamma + p_\gamma)\nabla\Psi.
 \end{aligned} \tag{97}$$

This equation takes the same form as the photon-dominated system except for the $(1+R)$ terms which multiply everything but the pressure gradient terms since the pressure comes predominantly from the photons. We can rewrite the equation more compactly as

$$[(1+R)v_{\gamma b}]' = k\Theta + (1+R)k\Psi. \tag{98}$$

Oscillator with Gravity and Baryons — The photon continuity equation (80) remains the same so that the oscillator equation becomes

$$[(1+R)\dot{\Theta}]' + \frac{1}{3}k^2\Theta = -\frac{1}{3}k^2(1+R)\Psi - [(1+R)\dot{\Phi}]'. \tag{99}$$

This equation is the final oscillator equation for the tight coupling or perfect fluid regime.

We can make several simplifications to illuminate the impact of baryons. First let us continue to use the matter dominated approximation where $\Psi = -\Phi = \text{const}$. Next let us make the adiabatic approximation where the change in R is slow compared with the frequency of oscillation $\dot{R}/R \ll \omega = kc_s$. In that case, Eqn. (99) looks like an oscillator equation with a fractional change in the mass given by R and a change in the sound speed

$$c_s^2 = \frac{\dot{p}_\gamma + \dot{p}_b}{\dot{\rho}_\gamma + \dot{\rho}_b} = \frac{1}{3(1+R)}. \tag{100}$$

Consequently, the solution in Eqn. (86) is modified as

$$[\Theta + (1+R)\Psi](\eta) = [\Theta + (1+R)\Psi](0) \cos ks. \tag{101}$$

This solution is reminiscent of that of adding mass to the spring in a constant gravitational field of the earth.

There are 3 effects of baryon loading. First the amplitude of oscillations increases by a factor of $1+3R$

$$[\Theta + (1+R)\Psi](0) = \frac{1}{3}(1+3R)\Psi(0). \tag{102}$$

Next the equilibrium point of the oscillation is now shifted so that relative to zero effective temperature, the even and odd peaks have different amplitudes

$$\begin{aligned}
 [\Theta + \Psi]_n &= [\pm(1+3R) - 3R]\frac{1}{3}\Psi(0), \\
 [\Theta + \Psi]_1 - [\Theta + \Psi]_2 &= [-6R]\frac{1}{3}\Psi(0).
 \end{aligned} \tag{103}$$

In particular, baryon loading increases the heights of the odd peaks over the even peaks (see Fig. 12).

Finally, the lowering of the sound speed changes the acoustic scale in Eqn. (69) as

$$\ell_A \propto \sqrt{1+R}. \tag{104}$$

The effects of baryon loading in a full calculation are actually smaller since R is growing in time.

Baryon-Photon Momentum Ratio Evolution — One can get a handle on the effect of evolution of R

by again equating the system to the analogous physical oscillator. The baryons add inertia or mass to the system and for a slowly varying mass the oscillator equation has an adiabatic invariant

$$\frac{E}{\omega} = \frac{1}{2} m_{\text{eff}} \omega A^2 = \frac{1}{2} (1 + R) k c_s A^2 \propto A^2 (1 + R)^{1/2} = \text{const.} \quad (105)$$

Amplitude of oscillation $A \propto (1 + R)^{-1/4}$ decays adiabatically as the photon-baryon ratio changes. This offsets the gain in the overall amplitude from Eqn. (102). Coupled with uncertainties in the distance to recombination in interpreting the ℓ_A measurement, this leaves the modulation of the peak heights as the effect that provides most of the information about the baryon-photon ratio in the acoustic peaks.

3.5 Matter-Radiation Ratio

Next we want to go beyond the matter-dominated expansion approximation. The universe only becomes matter dominated in the few e-folds before recombination (see Eqn. (48)). Peaks corresponding to wavenumbers that began oscillating earlier carry the effects of the prior epoch of radiation domination. These effects come in through the evolution of the gravitational potential which acts as a forcing function on the oscillator through Eqn. (99).

Potential Decay — The argument given in §3.3 for the constancy of the gravitational potential depends crucially on gravity being the dominant force affecting the total density. When radiation dominates the total density, radiation stresses become more important than gravity on scales smaller than the sound horizon. The total density fluctuation stops growing and instead oscillates with the acoustic frequency. The Poisson equation in the radiation dominated epoch

$$k^2 \Phi = 4\pi G a^2 \rho_r \Delta_r \quad (106)$$

then implies that Φ oscillates and decays with an amplitude $\propto a^{-2}$ (see Fig. 11). As an aside, the relativistic stresses of dark energy make the gravitational potential decay again during the acceleration epoch and lead to the so called integrated Sachs-Wolfe effect.

Radiation Driving — An examination of Fig. 11 shows that the time evolution of the gravitational potential is in phase with the acoustic oscillations themselves and act a driving force on the acoustic oscillations. We can estimate the effect on the amplitude of oscillations in the limit that the force is fully coherent. In that case we can take the continuity equation (80) and simply integrate it

$$\begin{aligned} [\Theta + \Psi](\eta) &= [\Theta + \Psi](0) + \Delta\Psi - \Delta\Phi \\ &= \frac{1}{3}\Psi(0) - 2\Psi(0) = \frac{5}{3}\Psi(0). \end{aligned} \quad (107)$$

This estimate gives an acoustic amplitude that is $5\times$ that of the Sachs-Wolfe effect. This enhancement only occurs for modes that begin oscillating during the radiation dominated epoch, *i.e.* the higher peaks. The net effect is a gradual ramp up of the acoustic oscillation amplitude across the horizon wavenumber at matter radiation equality (see Fig. 10).

In fact the coherent approximation is exact for a photon-baryon fluid but must be corrected for the neutrino contribution to the radiation density.

External Potential Approach — For pedagogical purposes it is sometimes useful to go beyond the coherent approximation. Neutrino corrections are one example; isocurvature initial conditions are another.

We have seen that the solutions to homogeneous equation for the oscillator equation (82) are

$$(1 + R)^{-1/4} \cos(ks), \quad (1 + R)^{-1/4} \sin(ks) \quad (108)$$

in the adiabatic or high frequency limit. Considering the potentials as external, we can solve for the temperature perturbation as (Hu and Sugiyama 1995)

$$(1 + R)^{1/4} \Theta(\eta) = \Theta(0) \cos(ks) + \frac{\sqrt{3}}{k} \left[\dot{\Theta}(0) + \frac{1}{4} \dot{R}(0) \Theta(0) \right] \sin ks \\ + \frac{\sqrt{3}}{k} \int_0^\eta d\eta' (1 + R')^{3/4} \sin[ks - ks'] F(\eta'), \quad (109)$$

where

$$F = -\ddot{\Phi} - \frac{\dot{R}}{1 + R} \dot{\Phi} - \frac{k^2}{3} \Psi. \quad (110)$$

By including the neutrino effects in the gravitational potential, we can show from this approach that radiation driving actually creates an acoustic amplitude that is close to $4 \times$ the Sachs-Wolfe effect.

3.6 Damping

The final piece in the acoustic oscillation puzzle is the damping of power beyond $\ell \sim 10^3$ shown in Fig. 6. Up until this point, we have considered the oscillations in the tight coupling approximation where the photons and baryons respond to pressure and gravity as a single perfect fluid. Fluid imperfections are associated with the Compton mean free path in Eqn. (46). Dissipation becomes strong at the diffusion scale, the distance a photon can random walk in a given time η (Silk 1968)

$$\lambda_D = \sqrt{N} \lambda_C = \sqrt{\eta / \lambda_C} \lambda_C = \sqrt{\eta \lambda_C}. \quad (111)$$

This scale is the geometric mean between the horizon and mean free path. Given that $\lambda_D / \eta_* \sim$ few percent, we expect that the $n \geq 3$ peaks to be affected by dissipation. To improve on this estimate, we develop the microphysical description of dissipation next.

Continuity Equations — To treat the photons and baryons as separate systems, we now need to supplement the photon continuity equation with the baryon continuity equation

$$\dot{\Theta} = -\frac{k}{3} v_\gamma - \dot{\Phi}, \quad \dot{\delta}_b = -k v_b - 3\dot{\Phi}. \quad (112)$$

The baryon equation follows from number conservation with $\rho_b = m_b n_b$ and $\delta_b \equiv \delta \rho_b / \rho_b$.

Euler and Navier-Stokes Equations — The momentum conservation equations must also be separated into photon and baryon pieces

$$\dot{v}_\gamma = k(\Theta + \Psi) - \frac{k}{6} \pi_\gamma - \dot{\tau}(v_\gamma - v_b), \\ \dot{v}_b = -\frac{\dot{a}}{a} v_b + k\Psi + \dot{\tau}(v_\gamma - v_b)/R,$$

where the photons gain an anisotropic stress term π_γ from radiation viscosity. The baryon equation follows from the same derivation as in §3.2 where the redshift of the momentum is carried by the bulk velocity instead of the redshifting temperature. Finally there is a momentum exchange term from Compton scattering. Note that the total momentum in the system is conserved and hence the scattering terms come with opposite sign.

Viscosity — Radiative shear viscosity is equivalent to quadrupole moments in the temperature field. These quadrupole moments are generated by radiation streaming from hot to cold regions much like how temperature inhomogeneity are converted to anisotropy in Fig. 8.

In the tight coupling limit where $\dot{\tau}/k$, the optical depth through a wavelength of the fluctuation is high one therefore expects

$$\pi_\gamma \sim v_\gamma \frac{k}{\dot{\tau}}, \quad (113)$$

since it must be generated by streaming and suppressed by scattering. A more detailed calculation from the Boltzmann or radiative transfer equation says (Kaiser 1983)

$$\pi_\gamma \approx 2A_v v_\gamma \frac{k}{\dot{\tau}}, \quad (114)$$

where $A_v = 16/15$ once polarization effects are incorporated

$$\dot{v}_\gamma = k(\Theta + \Psi) - \frac{k}{3} A_v \frac{k}{\dot{\tau}} v_\gamma. \quad (115)$$

The oscillator equation with viscosity becomes

$$c_s^2 \frac{d}{d\eta} (c_s^{-2} \dot{\Theta}) + \frac{k^2 c_s^2}{\dot{\tau}} A_v \dot{\Theta} + k^2 c_s^2 \Theta = -\frac{k^2}{3} \Psi - c_s^2 \frac{d}{d\eta} (c_s^{-2} \dot{\Phi}),$$

As in a mechanical oscillator, a term that depends on $\dot{\Theta}$ provides a dissipational term to the solutions.

Heat Conduction — Relative motion between the photons and baryons also damp oscillations. By expanding the continuity and momentum conservation equations in the small number $k/\dot{\tau}$ one obtains for the full oscillator equation

$$c_s^2 \frac{d}{d\eta} (c_s^{-2} \dot{\Theta}) + \frac{k^2 c_s^2}{\dot{\tau}} [A_v + A_h] \dot{\Theta} + k^2 c_s^2 \Theta = -\frac{k^2}{3} \Psi - c_s^2 \frac{d}{d\eta} (c_s^{-2} \dot{\Phi})$$

where

$$A_h = \frac{R^2}{1+R}. \quad (116)$$

Dispersion Relation — We can solve the damped oscillator equation in the adiabatic approximation by taking a trial solution $\Theta \propto \exp(i \int \omega d\eta)$ to obtain the dispersion relation

$$\omega = \pm k c_s \left[1 \pm \frac{i}{2} \frac{k c_s}{\dot{\tau}} (A_v + A_h) \right]. \quad (117)$$

The imaginary term in the dispersion relation gives an exponential damping of the oscillation amplitude

$$\begin{aligned} \exp(i \int \omega d\eta) &= e^{\pm i k s} \exp\left[-k^2 \int d\eta \frac{1}{2} \frac{c_s^2}{\dot{\tau}} (A_v + A_h)\right] \\ &= e^{\pm i k s} \exp[-(k/k_D)^2], \end{aligned} \quad (118)$$

where the diffusion wavenumber is given by

$$k_D^{-2} = \int d\eta \frac{1}{\dot{\tau}} \frac{1}{6(1+R)} \left(\frac{16}{15} + \frac{R^2}{(1+R)} \right). \quad (119)$$

Note that in both the high and low R limits

$$\begin{aligned}\lim_{R \rightarrow 0} k_D^{-2} &= \frac{1}{6} \frac{16}{15} \int d\eta \frac{1}{\dot{\tau}}, \\ \lim_{R \rightarrow \infty} k_D^{-2} &= \frac{1}{6} \int d\eta \frac{1}{\dot{\tau}}.\end{aligned}\tag{120}$$

Hence the dissipation scale is

$$\lambda_D = \frac{2\pi}{k_D} \sim \frac{2\pi}{\sqrt{6}} (\eta \dot{\tau}^{-1})^{1/2}\tag{121}$$

and comparable to the geometric mean between horizon and mean free path as expected from the random walk argument. For a baryon density of $\Omega_b h^2 \approx 0.02$, radiation viscosity is responsible for most of the dissipation and we show the correspondence between viscosity generation and dissipation in Fig. 11.

Since the diffusion length changes rapidly through recombination and the medium changes from optically thick to optically thin, the damping estimates above are only qualitative. A full Boltzmann (radiative transfer solution) shows a more gradual, but still exponential, damping of roughly

$$\mathcal{D}_\ell \approx \exp[-(\ell/\ell_D)^{1.25}],\tag{122}$$

with a damping scale of $\ell_D = 2\pi D_*/\lambda_D$ and (Hu 2005)

$$\frac{\lambda_D}{\text{Mpc}} \approx 64.5 \left(\frac{\Omega_m h^2}{0.14} \right)^{-0.278} \left(\frac{\Omega_b h^2}{0.024} \right)^{-0.18},\tag{123}$$

for small changes around the central values of $\Omega_m h^2$ and $\Omega_b h^2$.

This envelope also accounts for enhanced damping due to the finite duration of recombination. Instead of a delta function in the projection equation (31) we have the visibility function $\dot{\tau} e^{-\tau}$ that acts as a smearing out of any contributions with wavelengths shorter than the thickness of the recombination surface that survive dissipation.

3.7 Information from the Peaks

In the preceding sections we have examined the physical processes involved in the formation of the acoustic peaks and explained their sensitivity to the energy content and expansion rate of the universe. Converting the measurements into parameter constraints of course requires a more accurate numerical description. Numerical codes that solve the Einstein-Boltzmann radiative transfer equations for the CMB and matter (Peebles and Yu 1970; Bond and Efstathiou 1984; Vittorio and Silk 1984) are now accurate at the $\sim 1\%$ level for the acoustic peaks for publically available codes (Seljak and Zaldarriaga 1996; Lewis et al. 2000). Their numerical precision on the other hand is substantially better and approaches the 0.1% level required for cosmic variance limited measurements out to $\ell \sim 10^3$. The accuracy is now limited by the input physics, mainly recombination (see 2.3). In this section, we relate the qualitative discussion of the previous sections to the quantitative information content of the peaks.

First Peak: Curvature and Dark Energy — The comparison between the predicted acoustic peak scale λ_A and its angular extent provides a measurement of the angular diameter distance to recombination. The angular diameter distance in turn depends on the spatial curvature and expansion history of the universe.

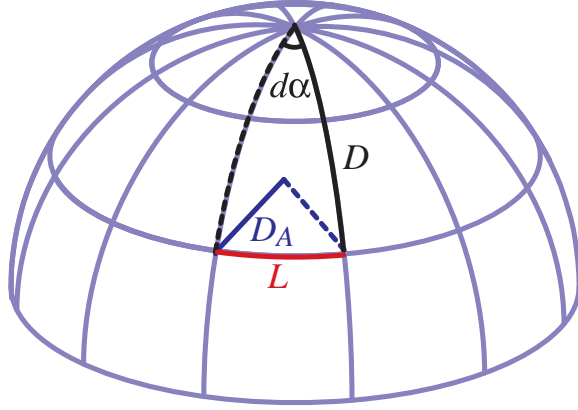


Fig. 13. Angular diameter distance and curvature. In a non-flat (here closed) universe, the apparent or angular diameter distance $D_A = Ld\alpha$ does not equal the radial distance traveled by the photon. Objects in a closed universe are further than they appear whereas in an open universe they are closer than they appear.

Sensitivity to the expansion history during the acceleration epoch comes about through the radial distance a photon travels along the line of sight

$$D_* = \int_0^{z_*} \frac{dz}{H(z)} = \eta_0 - \eta_* . \quad (124)$$

With the matter and radiation energy densities measured, the remaining contributor to the expansion rate $H(z)$ is the dark energy.

However in a curved universe, the apparent or angular diameter distance D_A in Eqn. (69) is no longer the distance a photon travels radially along the line of sight. The radius of curvature of the space is given in terms of the total density Ω_{tot} in units of the critical density as

$$R^{-2} = H_0^2(\Omega_{\text{tot}} - 1) . \quad (125)$$

A positive curvature space has $\Omega_{\text{tot}} > 1$ and a real radius of curvature. A negatively curved space has $\Omega_{\text{tot}} < 1$ and an imaginary radius of curvature. The positively curved space is shown in Fig. 13. The curvature makes a transverse distance L related to its angular extent $d\alpha$ as $L = d\alpha D_A$ with

$$D_A = R \sin(D/R) . \quad (126)$$

The same formula applies for negatively curved spaces but is more conveniently expressed with the relation

$$R \sin(D/R) = |R| \sinh(D/|R|) \quad (127)$$

for imaginary R . In a positively curved geometry $D_A < D$ and objects are further than they appear. In a negatively curved universe R is imaginary and $R \sin(D/R) = i|R| \sin(D/i|R|) = |R| \sinh(D/|R|)$ – and $D_A > D$ objects are closer than they appear. Since the detection of the first acoustic peak it has been clear that the universe is close to spatially flat (Miller et al. 1999; de Bernardis et al. 2000; Hanany et al. 2000). How close and how well-measured D_* is for dark energy studies depends on the calibration of the physical scale $\lambda_A = 2s_*$, i.e. the sound horizon at recombination.

The sound horizon in turn depends on two things,

$$s_* = \frac{2\sqrt{3}}{3} \sqrt{\frac{a_*}{R_* \Omega_m H_0^2}} \ln \frac{\sqrt{1+R_*} + \sqrt{R_* + r_* R_*}}{1 + \sqrt{r_* R_*}} , \quad (128)$$

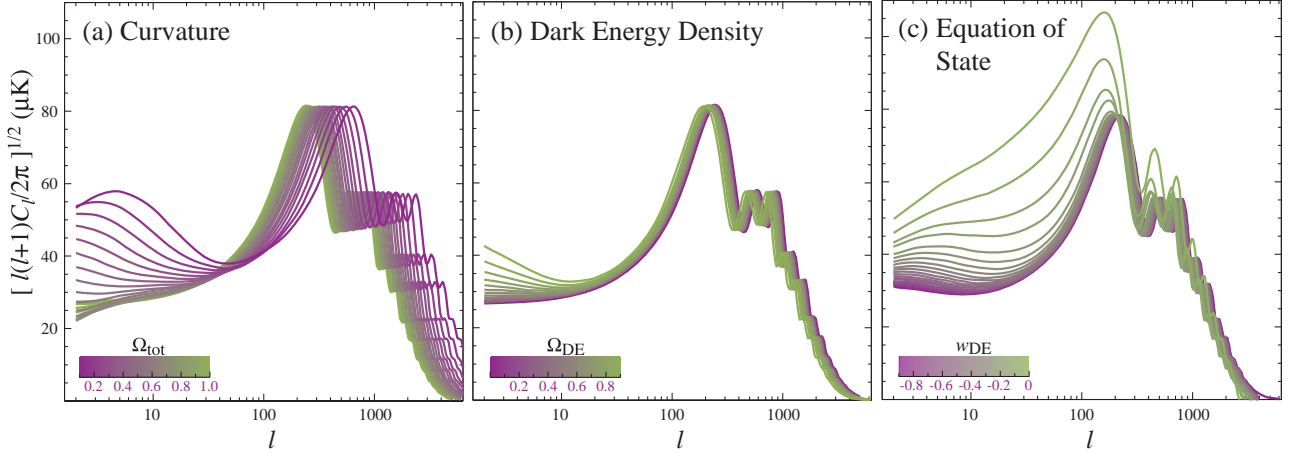


Fig. 14. Curvature and dark energy. Given a fixed physical scale for the acoustic peaks (fixed $\Omega_b h^2$ and $\Omega_m h^2$) the observed angular position of the peaks provides a measure of the angular diameter distance and the parameters it depends on: curvature, dark energy density and dark energy equation of state. Changes at low ℓ multipoles are due to the decay of the gravitational potential after matter domination from the integrated Sachs-Wolfe effect.

the baryon-photon momentum density ratio

$$R_* \equiv \frac{3}{4} \frac{\rho_b}{\rho_\gamma} \Big|_{a_*} = 0.729 \left(\frac{\Omega_b h^2}{0.024} \right) \left(\frac{a_*}{10^{-3}} \right), \quad (129)$$

and the expansion rate prior to recombination which is determined by the matter radiation ratio

$$r_* \equiv \frac{\rho_r}{\rho_m} \Big|_{a_*} = 0.297 \left(\frac{\Omega_m h^2}{0.14} \right)^{-1} \left(\frac{a_*}{10^{-3}} \right)^{-1}. \quad (130)$$

The calibration of these two quantities involves the higher acoustic peaks. The bottom line is that the limiting factor in the calibration is the precision with which the matter density is known

$$\frac{\delta D_{A*}}{D_{A*}} \approx \frac{1}{4} \frac{\delta(\Omega_m h^2)}{\Omega_m h^2}. \quad (131)$$

In principle the Planck satellite can achieve a 1% measurement of the matter density or a $\sim 0.25\%$ measure of distance. Current errors on the distance are $\sim 1\text{-}2\%$.

Second Peak: Baryons — The baryon-photon ratio controls the even-odd modulation of peak heights through the baryon loading effect (see §3.4). The second peak represents rarefaction of the acoustic wave in a gravitational potential and hence is suppressed in amplitude by the baryon inertia. The dependence of the spectrum on the baryon density $\Omega_b h^2$ is shown in Fig. 15. Since the first tentative detection of the second peak (de Bernardis et al. 2000) the CMB has placed limits on the baryon density. Currently its measurement, largely from WMAP (Spergel et al. 2007), gives $\Omega_b h^2 = 0.0227 \pm 0.0006$ (Reichardt et al. 2008). This is well enough constrained that associated errors on the sound horizon and shape of the matter power spectrum (see below) are small.

Third Peak: Dark Matter — The third peak begins to show the effects of the matter-radiation ratio on the overall amplitude of the acoustic peaks. Furthermore, decay in the gravitational potential during radiation domination would reduce the baryon loading effect and change the peak height ratios of the

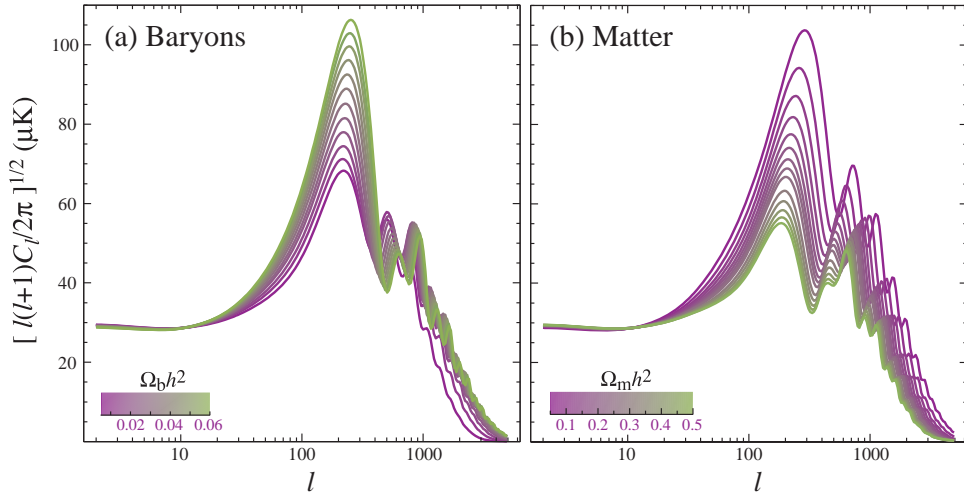


Fig. 15. Baryons and matter. Baryons change the relative heights of the even and odd peaks through their inertia in the plasma. The matter-radiation ratio also changes the overall amplitude of the oscillations from driving effects. Adapted from Hu and Dodelson (2002).

second and third peaks (*e.g.* Hu et al. 2001). The dependence of the spectrum on the baryon density $\Omega_b h^2$ is shown in Fig. 15. Constraints on the third peak from the DASI experiment (Pryke et al. 2001) represented the first direct evidence for dark matter at the epoch of recombination. Current constraints from a combination of WMAP and higher resolution ground and balloon based data yield $\Omega_m h^2 = 0.135 \pm 0.007$ (Reichardt et al. (2008)). Since this parameter controls the error on the distance to recombination through equation (131) and the matter power spectrum (see below), it is important to improve the precision of its measurement with the third higher peaks.

Damping Tail: Consistency— Under the standard thermal history of §2 and matter content, the parameters that control the first 3 peaks also determine the structure of the damping tail at $\ell > 10^3$: namely, the angular diameter distance to recombination D_* , the baryon density $\Omega_b h^2$ and the matter density $\Omega_m h^2$. When the damping tail was first discovered by the CBI experiment (Padin et al. 2001), it supplied compelling support for the standard theoretical modeling of the physics at recombination outlined here. Currently the best constraints on the damping tail are from the ACBAR experiment (Reichardt et al. 2008, see Fig. 7). Consistency between the low order peaks and the damping tail can be used to make precision tests of recombination and any physics beyond the standard model at that epoch. For example, damping tail measurements can be used to constrain the evolution of the fine structure constant.

Matter Power Spectrum: Shape & Amplitude — The acoustic peaks also determine the shape and amplitude of the matter power spectrum. Firstly, acoustic oscillations are shared by the baryons. In particular, the plasma motion kinematically produces enhancements of density near recombination (see Eqn. 113))

$$\delta_b \approx -k\eta_* v_b(\eta_*) \approx -k\eta_* v_\gamma(\eta_*). \quad (132)$$

This enhancement then imprints into the matter power spectrum at an amplitude reduced by ρ_b/ρ_m due to the small baryon fraction (Hu and Sugiyama 1996). Secondly, the gravitational potentials that the cold dark matter perturbations fall in are evolving through the plasma epoch due to the

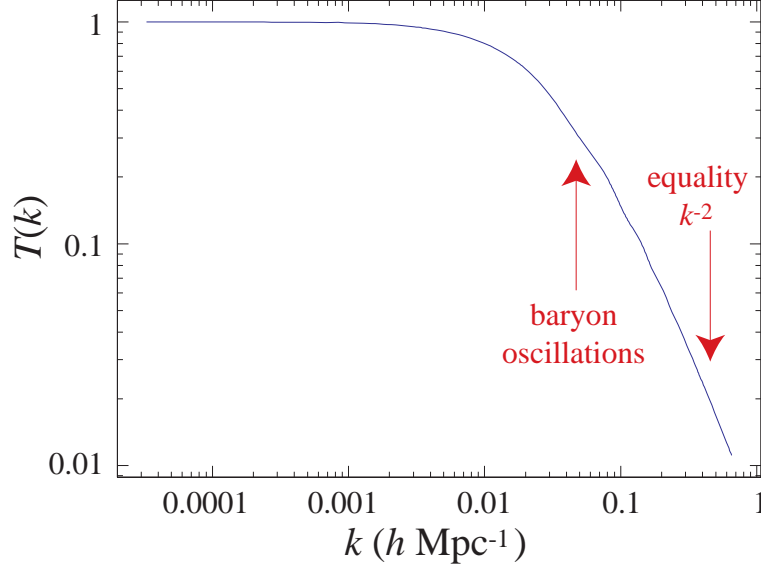


Fig. 16. Transfer function. Acoustic and radiation physics is imprinted on the matter power spectrum as quantified by the transfer function $T(k)$. The former is responsible for baryon oscillations in the spectrum and the latter a suppression of growth due to Jeans stability for scales smaller than the horizon at matter-radiation equality.

processes described in §3.5. On scales above the horizon, relativistic stresses are never important and the gravitational potential remains constant. The Poisson equation then implies that

$$\Delta \sim (k\eta)^2 \Phi(0), \quad (133)$$

and in particular, the density perturbation at horizon crossing where $k\eta \sim 1$ is $\Delta = \Delta_H \approx \Phi(0)$. For a fluctuation that crosses the horizon during radiation domination, the total density perturbation is Jeans stabilized until matter radiation equality

$$\eta_{\text{eq}} \approx 114 \left(\frac{\Omega_m h^2}{0.14} \right)^{-1} \text{Mpc}. \quad (134)$$

Thereafter, relativistic stresses again become irrelevant and the potential remains unchanged until matter ceases to dominate the expansion

$$\Phi \approx (k\eta_{\text{eq}})^{-2} \Delta_H \sim (k\eta_{\text{eq}})^{-2} \Phi(0). \quad (135)$$

The transfer in shape from the initial conditions due to baryon oscillations and matter radiation equality is usually encapsulated into a transfer function $T(k)$. Given an initial power spectrum of the form (94), the evolution through to matter domination transforms the potential power spectrum to $k^3 P_\Phi / 2\pi^2 \propto k^{n-1} T^2(k)$ where $T(k) \propto k^{-2}$ beyond the wavenumber at matter-radiation equality. This scaling is slightly modified due to the logarithmic growth of dark matter fluctuations during the radiation epoch when the radiation density is Jeans stable. The matter power spectrum and potential power spectrum are related by the Poisson equation and so carry the same shape. Specifically

$$\frac{k^3 P_m(k, a)}{2\pi^2} = \frac{4}{25} \delta_\zeta^2 \left(\frac{G(a)a}{\Omega_m} \right)^2 \left(\frac{k}{H_0} \right)^4 \left(\frac{k}{k_{\text{norm}}} \right)^{n-1} T^2(k), \quad (136)$$

where we have included a factor $G(a)$ to account for the decay in the potential during the acceleration

epoch when relativistic stresses are again important (see e.g. Hu (2005)). This factor only depends on time and not scale as long as the scale in question is within the Jeans scale of the accelerating component. In this limit, $G(a)$ is determined by the solution to

$$\frac{d^2 G}{d \ln a^2} + \left(4 + \frac{d \ln H}{d \ln a}\right) \frac{dG}{d \ln a} + \left[3 + \frac{d \ln H}{d \ln a} - \frac{3}{2} \Omega_m(a)\right] G = 0, \quad (137)$$

with an initial conditions of $G(\ln a_{\text{md}}) = 1$ and $G'(\ln a_{\text{md}}) = 0$ at an epoch a_{md} when the universe is fully matter dominated.

The transfer function $T(k)$, with k in Mpc^{-1} , depends only on the baryon density $\Omega_b h^2$ and the matter density $\Omega_m h^2$ which are well determined by the CMB acoustic peaks. Features in the matter power spectrum, especially the baryon oscillations, then serve as standard rulers for distance measurements Eisenstein et al. (1998). For example, its measurement in a local redshift survey where the distance is calibrated in $h \text{ Mpc}^{-1}$ would give the Hubble constant h . Detection of the features requires a Gpc^3 of volume and so precise, purely local, measurements are not feasible. Nonetheless, the first detection of these oscillations by the SDSS LRG redshift survey out to $z \sim 0.4$ provide remarkably tight constraints on the acceleration of the expansion (Eisenstein et al. 2005).

The CMB also determines the initial normalization δ_ζ and so provides a means by which to test the effect of the acceleration on the growth function $G(a)$. The precision of this determination is largely set by reionization. The opacity provided by electrons after reionization suppress the observed amplitude of the peaks relative to the initial amplitude and hence

$$\delta_\zeta \approx 4.6e^{-(0.1-\tau)} \times 10^{-5}, \quad (138)$$

where τ is the optical depth to recombination. Note that this is the normalization at $k = 0.05 \text{ Mpc}^{-1}$ and even with uncertainties in the optical depth of $\delta\tau \sim 0.03$ it exceeds the precision of the COBE normalization (*c.f.* Eqn. (95)). Finally, with the matter and baryon transfer effects determined, the acoustic spectrum also constrains the tilt. WMAP provided the first hints of a small deviation from scale invariance (Spergel et al. 2007) and the current constraints are $n \approx 0.965 \pm 0.015$.

Combining these factors into the conventional measure of the amplitude of matter fluctuations today

$$\begin{aligned} \sigma_8^2 &\equiv \int \frac{dk}{k} \frac{k^3 P(k, a=1)}{2\pi^2} W_\sigma^2(kr) \\ \sigma_8 &\approx \frac{\delta_\zeta}{5.59 \times 10^{-5}} \left(\frac{\Omega_b h^2}{0.024}\right)^{-1/3} \left(\frac{\Omega_m h^2}{0.14}\right)^{0.563} \\ &\quad \times (3.123h)^{(n-1)/2} \left(\frac{h}{0.72}\right)^{0.693} \frac{G_0}{0.76}, \end{aligned} \quad (139)$$

where $W_\sigma(x) = 3x^{-3}(\sin x - x \cos x)$ is the Fourier transform of a top hat window of radius $r = 8h^{-1}\text{Mpc}$.

4 Polarization Anisotropy from Recombination

Thomson scattering of quadrupolarly anisotropic but unpolarized radiation generates linear polarization. As we have seen in §3.1, $\ell \geq 2$ anisotropy develops only in optically thin conditions. Given that polarization also requires scattering to be generated, the polarization anisotropy is generically much smaller than the temperature anisotropy. The main source of polarization from recombination

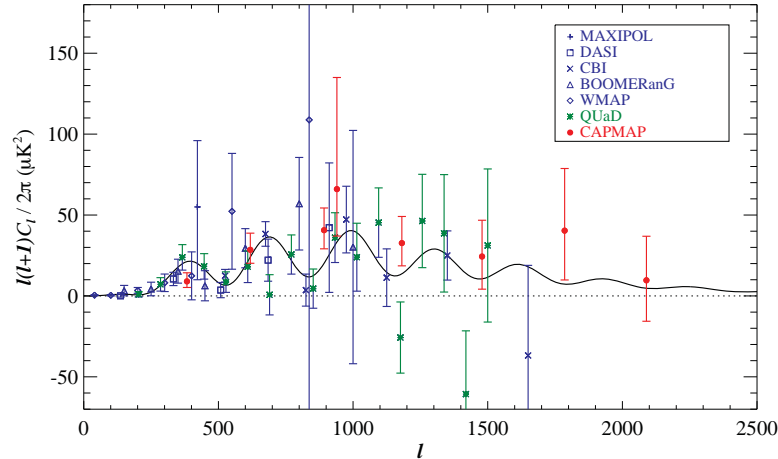


Fig. 17. E -mode polarization power spectrum measurements. Adapted from Bischoff et al. (2008)

is associated with the acoustic peaks in temperature. This source was first detected by the DASI experiment (Kovac et al. 2002) and recent years have seen increasingly precise measurements (see Fig. 17).

Since acoustic polarization arises from linear scalar perturbations, they possess a symmetry that relates the direction of polarization to the wavevector or change in the polarization amplitude. As we shall see in the next section, this symmetry is manifest in the absence of B -modes (Kamionkowski et al. 1997; Zaldarriaga and Seljak 1997). B -modes at recombination can be generated from the quadrupole moment of a gravitational wave. This yet-to-be-detected signal would be invaluable for early universe studies involving the inflationary origin of perturbations.

We begin by reviewing the Stokes parameter description of polarization (§4.1) and its relation to E and B harmonic representation (§4.2). We continue with a discussion of polarized Thomson scattering in §4.3. In §4.4 and 4.5 we discuss the polarization signatures of acoustic oscillations and gravitational waves.

4.1 Statistical Description

The polarization field can be analyzed in a way very similar to the temperature field, save for one complication. In addition to its strength, polarization also has an orientation, depending on relative strength of two linear polarization states.

The polarization field is defined locally in terms of Stokes parameters. In general, the polarization state of radiation in direction $\hat{\mathbf{n}}$ described by the intensity matrix $\langle E_i(\hat{\mathbf{n}})E_j^*(\hat{\mathbf{n}}) \rangle$, where \mathbf{E} is the electric field vector in the transverse plane and the brackets denote time averaging. As a 2×2 hermitian matrix, it can be decomposed into the Pauli basis

$$\begin{aligned} \mathbf{P} &= C \langle \mathbf{E}(\hat{\mathbf{n}}) \mathbf{E}^\dagger(\hat{\mathbf{n}}) \rangle \\ &= \Theta(\hat{\mathbf{n}}) \boldsymbol{\sigma}_0 + Q(\hat{\mathbf{n}}) \boldsymbol{\sigma}_3 + U(\hat{\mathbf{n}}) \boldsymbol{\sigma}_1 + V(\hat{\mathbf{n}}) \boldsymbol{\sigma}_2, \end{aligned} \quad (140)$$

where

$$\begin{aligned}\boldsymbol{\sigma}_0 &= \begin{pmatrix} 1 & 0 \\ 0 & 1 \end{pmatrix}, & \boldsymbol{\sigma}_2 &= \begin{pmatrix} 0 & -1 \\ 1 & 0 \end{pmatrix} i, \\ \boldsymbol{\sigma}_1 &= \begin{pmatrix} 0 & 1 \\ 1 & 0 \end{pmatrix}, & \boldsymbol{\sigma}_3 &= \begin{pmatrix} 1 & 0 \\ 0 & -1 \end{pmatrix}.\end{aligned}\tag{141}$$

Orthogonality of the Pauli matrices says that the Stokes parameters are recovered from the polarization matrix as $\text{Tr}(\sigma_i \mathbf{P})/2$. The Stokes Q and U parameter define the linear polarization state whereas V defines the circular polarization state. We have chosen the proportionality constant so that all the Stokes parameters are in temperature fluctuation units.

From this description, we see that Q represents polarization aligned with one of the principal axes of the transverse coordinate system whereas U represents polarization at 45° to these axes.

4.2 *EB Harmonic Description*

The disadvantage of the Stokes Q and U representation is that the distinction between the two depends on the coordinate system for the two transverse directions on the sky. Under a rotation of this basis by θ

$$Q' \pm iU' = e^{\mp 2i\theta} [Q \pm iU].\tag{142}$$

For a harmonic decomposition, it is more useful to choose this basis to be given by the wavevector itself. For small sections of the sky, the harmonic decomposition becomes a Fourier transform and we can define the E and B harmonics as

$$\begin{aligned}E(\mathbf{l}) \pm iB(\mathbf{l}) &= \int d\hat{\mathbf{n}} [Q'(\hat{\mathbf{n}}) \pm iU'(\hat{\mathbf{n}})] e^{-i\mathbf{l}\cdot\hat{\mathbf{n}}} \\ &= e^{\mp 2i\phi_1} \int d\hat{\mathbf{n}} [Q(\hat{\mathbf{n}}) \pm iU(\hat{\mathbf{n}})] e^{-i\mathbf{l}\cdot\hat{\mathbf{n}}},\end{aligned}\tag{143}$$

where in the second line we have rotated Q and U back to a fixed coordinate system with the angle ϕ_1 that the Fourier vector makes with the \mathbf{x} axis.

For linear scalar fluctuations, we have seen that the only direction for a given harmonic mode is set by the direction of the wavevector itself: velocity fields point in this direction or its opposite, quadrupole moments are symmetric about this axis, etc. This means that symmetry requires that such sources only generate Q' or E for each mode. This symmetry also holds once all the modes are superimposed back to the full polarization field: linear scalar perturbations generate only E -modes where the polarization direction is related to the direction in which the polarization amplitude changes.

To generalize this decomposition to the full curved sky, we need to replace plane waves, the tensor eigenfunctions of the Laplace operator in a flat space, to the correct tensor eigenfunctions for the curved space. These are called the spin-2 spherical harmonics:

$$\nabla_{\pm 2}^2 Y_{\ell m}[\boldsymbol{\sigma}_3 \mp i\boldsymbol{\sigma}_1] = -[l(l+1) - 4]_{\pm 2} Y_{\ell m}[\boldsymbol{\sigma}_3 \mp i\boldsymbol{\sigma}_1].\tag{144}$$

They obey the usual orthogonality and completeness relations

$$\begin{aligned}\int d\hat{\mathbf{n}}_s Y_{\ell m}^*(\hat{\mathbf{n}})_s Y_{\ell m}(\hat{\mathbf{n}}) &= \delta_{\ell\ell'} \delta_{mm'}, \\ \sum_{\ell m} {}_s Y_{\ell m}^*(\hat{\mathbf{n}})_s Y_{\ell m}(\hat{\mathbf{n}}') &= \delta(\phi - \phi') \delta(\cos\theta - \cos\theta').\end{aligned}\tag{145}$$

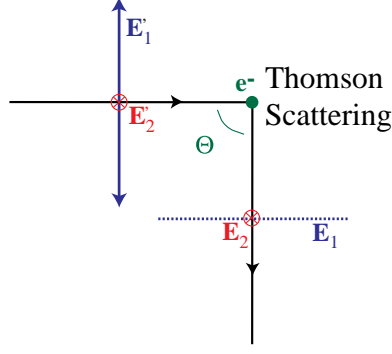


Fig. 18. Thomson scattering geometry. A quadrupole anisotropy in the incoming radiation leads to linear polarization. For scattering at $\Theta = \pi/2$, only one component of the initially unpolarized radiation (\mathbf{E}'_2) is scattered leaving one outgoing state (\mathbf{E}_1) unpopulated.

We can therefore decompose the linear polarization field just like the temperature field

$$[Q(\hat{\mathbf{n}}) \pm iU(\hat{\mathbf{n}})] = - \sum_{\ell m} [E_{\ell m} \pm iB_{\ell m}]_{\pm 2} Y_{\ell m}(\hat{\mathbf{n}}). \quad (146)$$

Likewise the power spectra are given by

$$\langle E_{\ell m}^* E_{\ell m} \rangle = \delta_{\ell\ell'} \delta_{mm'} C_{\ell}^{EE}, \quad (147)$$

$$\langle B_{\ell m}^* B_{\ell m} \rangle = \delta_{\ell\ell'} \delta_{mm'} C_{\ell}^{BB}, \quad (148)$$

and the cross correlation of E -polarization with temperature by

$$\langle \Theta_{\ell m}^* E_{\ell m} \rangle = \delta_{\ell\ell'} \delta_{mm'} C_{\ell}^{\Theta E}. \quad (149)$$

Other cross correlations vanish if parity is conserved.

4.3 Thomson Scattering

The differential cross section for Thomson scattering

$$\frac{d\sigma}{d\Omega} = \frac{3}{8\pi} |\hat{\mathbf{E}}' \cdot \hat{\mathbf{E}}|^2 \sigma_T, \quad (150)$$

is polarization dependent and hence scattering generates polarization. Here $\hat{\mathbf{E}}'$ and $\hat{\mathbf{E}}$ denote the incoming and outgoing directions of the electric field or polarization vector. Consider incoming radiation in the $\hat{\mathbf{x}}$ direction scattered at right angles into the $-\hat{\mathbf{y}}$ direction (see Fig. 18). Heuristically, incoming radiation shakes an electron in the direction of its electric field vector or polarization $\hat{\mathbf{e}}'$ causing it to radiate with an outgoing polarization parallel to that direction. However since the outgoing polarization $\hat{\mathbf{e}}$ must be orthogonal to the outgoing direction, incoming radiation that is polarized parallel to the outgoing direction cannot scatter leaving only one polarization state.

The incoming radiation however comes from all angles. If it were completely isotropic in intensity, radiation coming along the $\hat{\mathbf{z}}$ would provide the polarization state that is missing from that coming along $\hat{\mathbf{x}}$ leaving the net outgoing radiation unpolarized. Only a quadrupole temperature anisotropy in the radiation generates a net linear polarization from Thomson scattering. As we have seen, a quadrupole can only be efficiently generated if the universe is optically thin to Thomson scattering a given perturbation.

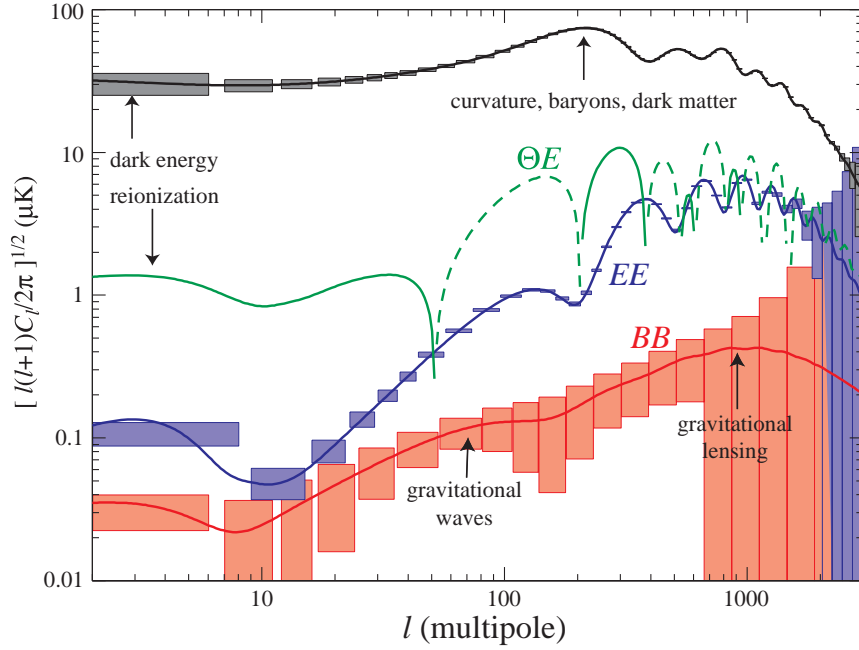


Fig. 19. Polarized landscape. While the E -spectrum and ΘE cross correlation are increasingly well measured, the B -spectrum from inflationary gravitational waves (shown here near the maximal value allowed by the temperature spectrum) and gravitational lensing remains undetected. Shown here are projected error bars associated with Planck sample variance and detector noise. Adapted from Hu and Dodelson (2002).

4.4 Acoustic Polarization

Acoustic oscillations in the dissipation regime provide the conditions necessary for polarization. Recall that radiative viscosity in the plasma is equivalent to quadrupole anisotropy in the photons. Since the quadrupole is of order (see Fig. 11)

$$\pi_\gamma \sim \frac{kv_\gamma}{\dot{\tau}} \sim \left(\frac{k}{k_D}\right) \frac{v_\gamma}{k_D \eta_*}, \quad (151)$$

the polarization spectrum rises as l/l_D to peak at the damping scale with an amplitude of about 10% of the temperature fluctuations before falling due to the elimination of the acoustic source itself due to damping. Since v_γ is out of phase with the temperature,

$$\Theta + \Psi \propto \cos(ks); \quad v_\gamma \propto \sin(ks), \quad (152)$$

the polarization peaks are also out of phase with the temperature peaks. Furthermore, the phase relation also tells us that the polarization is correlated with the temperature perturbations. The correlation power $C_l^{\Theta E}$ being the product of the two, exhibits oscillations at twice the acoustic frequency

$$(\Theta + \Psi)(v_\gamma) \propto \cos(ks) \sin(ks) \propto \sin(2ks). \quad (153)$$

As in the case of the damping, the predicting the precise value requires numerical codes (Bond and Efstathiou 1987) since $\dot{\tau}$ changes so rapidly near recombination. Nonetheless the detailed predictions bear these qualitative features.

Like the damping scale, the acoustic polarization spectrum is uniquely predicted from the temperature spectrum once $\Omega_b h^2$, $\Omega_m h^2$ and the initial conditions are specified. Polarization thus represents

a sharp test on the assumptions of the recombination physics and power law curvature fluctuations in the initial conditions used in interpreting the temperature peaks. For example, features in the initial power spectrum appear more distinct in the polarization than the temperature due to projection effects (see *e.g.* Hu and Okamoto (2004)).

4.5 Gravitational Waves

During the break down of tight coupling that occurs at last scattering, any gravitational waves present will also imprint a local quadrupole anisotropy to the photons and hence a linear polarization to the CMB (Polnarev 1985). These contribute to the BB power and their detection would provide invaluable information on the origin of the fluctuations. Specifically, in simple inflationary models their amplitude gives the energy scale of inflation. The gravitational wave amplitude h oscillates and decays once inside the horizon, so the associated polarization source scales as $\dot{h}/\dot{\tau}$ and so peaks at the $l \approx 100$ horizon scale and not the damping scale at recombination (see Fig. 19). This provides a useful scale separation of the various polarization effects.

If the energy scale of inflation is near the 10^{16} GeV scale then the signal is potentially detectable by the next generation of polarization experiments.

5 Discussion

The one and a half decades since the discovery of CMB anisotropy by COBE DMR has seen remarkable progress that ushered in the current epoch of precision cosmology. From the preliminary detections of degree scale power to the current measurements of 5 acoustic peaks, the damping tail and acoustic polarization, the milestones in the observational verification of our theoretical understanding of the universe at recombination have steadily been overtaken. Correspondingly, the measurements of the energy density contents of the universe at recombination and the distance to and hence expansion rate since recombination have improved from order unity constraints to several percent level determinations.

The next generation of experiments, including the Planck satellite and ground based polarization measurements, will push these determinations to the 1% level and beyond and perhaps detect the one outstanding prediction of the recombination epoch: the B -mode polarization of gravitational waves from inflation. Likewise the enhanced range of precision measurements of the power spectrum will bring measurements of the spectrum of scalar perturbations to the percent level and further test the physics of inflation.

Beyond the recombination epoch reviewed here, these experiments will also test secondary temperature and polarization anisotropy from reionization, lensing, and galaxy clusters as well as the Gaussianity of the initial conditions. Combined, these measurements will test the standard cosmological model with unprecedented precision.

Acknowledgments: I thank the organizers, R. Rebelo and J.A. Rubino-Martin, as well as the students of the XIX Canary Island Winter School of Astrophysics.

References

- Alpher, R.A. and Herman, R.C. (1948). On the relative abundance of the elements, *Phys. Rev.*, **74**, 1737–1742.
 Bardeen, J.M. (1980). Gauge invariant cosmological perturbations, *Phys. Rev.*, **D22**, 1882–1905.

- Bischoff, C. et al. (2008). New Measurements of Fine-Scale CMB Polarization Power Spectra from CAPMAP at Both 40 and 90 GHz. arXiv:0802.0888 [astro-ph].
- Bond, J.R. and Efstathiou, G. (1984). Cosmic background radiation anisotropies in universes dominated by nonbaryonic dark matter, *Astrophys. J. Lett.*, **285**, L45–L48.
- Bond, J.R. and Efstathiou, G. (1987). The statistics of cosmic background radiation fluctuations, *Mon. Not. R. Astron. Soc.*, **226**, 655–687.
- Danese, L. and de Zotti, G. (1982). Double Compton process and the spectrum of the microwave background, *Astron. Astrophys.*, **107**, 39–42.
- de Bernardis, P. et al. (2000). A flat Universe from high-resolution maps of the cosmic microwave background radiation, *Nature*, **404**, 955–959.
- Dicke, R.H., Peebles, P.J.E., Roll, P.G. and Wilkinson, D.T. (1965). Cosmic Black-Body Radiation., *Astrophys. J.*, **142**, 414–419.
- Eisenstein, D.J. et al. (2005). Detection of the Baryon Acoustic Peak in the Large-Scale Correlation Function of SDSS Luminous Red Galaxies, *Astrophys. J.*, **633**, 560–574. astro-ph/0501171.
- Eisenstein, D., Hu, W. and Tegmark, M. (1998). Cosmic Complementarity: H_0 and Ω_m from Combining CMB Experiments and Redshift Surveys, *Astrophys. J. Lett.*, **504**, L57. astro-ph/9805239.
- Fixsen, D.J. et al. (1996). The Cosmic Microwave Background Spectrum from the Full COBE FIRAS Data Set, *Astrophys. J.*, **473**, 576–587.
- Gamow, G. (1948). The origin of elements and the separation of galaxies, *Phys. Rev.*, **74**, 505–506.
- Hanany, S. et al. (2000). MAXIMA-1: A Measurement of the Cosmic Microwave Background Anisotropy on Angular Scales of 10^{-5} – 5° , *Astrophys. J. Lett.*, **545**, L5–L9.
- Hu, W. (2003). Covariant Linear Perturbation Formalism, *ICTP*, **14**, 149. astro-ph/0402060.
- Hu, W. (2005). Dark Energy Probes in Light of the CMB, *ASPC*, **339**, 215. astro-ph/0407158.
- Hu, W. and White, M.J. (2004). The cosmic symphony, *Sci. Am.*, **290N2**, 32–37.
- Hu, W. (1995). Wandering in the background: A Cosmic microwave background explorer. astro-ph/9508126.
- Hu, W. and Dodelson, S. (2002). Cosmic Microwave Background Anisotropies, *Ann. Rev. Astron. Astrophys.*, **40**, 171–216. astro-ph/0110414.
- Hu, W., Fukugita, M., Zaldarriaga, M. and Tegmark, M. (2001). CMB Observables and Their Cosmological Implications, *Astrophys. J.*, **549**, 669. astro-ph/0006436.
- Hu, W. and Okamoto, T. (2004). Principal Power of the CMB, *Phys. Rev.*, **D69**, 043004. astro-ph/0308049.
- Hu, W. and Silk, J. (1993). Thermalization and spectral distortions of the cosmic background radiation, *Phys. Rev.*, **D48**, 485–502.
- Hu, W. and Sugiyama, N. (1995). Anisotropies in the Cosmic Microwave Background: An Analytic Approach, *Astrophys. J.*, **444**, 489–506. astro-ph/9407093.
- Hu, W. and Sugiyama, N. (1996). Small scale cosmological perturbations: An Analytic approach, *Astrophys. J.*, **471**, 542–570. astro-ph/9510117.
- Hu, W. and White, M.J. (1996). A New Test of Inflation, *Phys. Rev. Lett.*, **77**, 1687–1690. astro-ph/9602020.
- Hu, W. and White, M.J. (1997). CMB Anisotropies: Total Angular Momentum Method, *Phys. Rev.*, **D56**, 596–615. astro-ph/9702170.
- Kaiser, N. (1983). Small-angle anisotropy of the microwave background radiation in the adiabatic theory, *Mon. Not. R. Astron. Soc.*, **202**, 1169–1180.
- Kamionkowski, M., Kosowsky, A. and Stebbins, A. (1997). Statistics of cosmic microwave background polarization, *Phys. Rev.*, **D55**, 7368–7388. astro-ph/9611125.
- Kovac, J. et al. (2002). Detection of polarization in the cosmic microwave background using DASI, *Nature*, **420**, 772–787. astro-ph/0209478.
- Lewis, A., Challinor, A. and Lasenby, A. (2000). Efficient Computation of Cosmic Microwave Background Anisotropies in Closed Friedmann-Robertson-Walker Models, *Astrophys. J.*, **538**, 473–476. arXiv:astro-ph/9911177.
- Mather, J.C., Fixsen, D.J., Shafer, R.A., Mosier, C. and Wilkinson, D.T. (1999). Calibrator Design for the COBE Far Infrared Absolute Spectrophotometer (FIRAS), *Astrophys. J.*, **512**, 511–520. astro-ph/9810373.
- Miller, A.D. et al. (1999). A Measurement of the Angular Power Spectrum of the Cosmic Microwave Background from $l = 100$ to 400, *Astrophys. J. Lett.*, **524**, L1–L4.
- Padin, S. et al. (2001). First Intrinsic Anisotropy Observations with the Cosmic Background Imager, *Astrophys. J. Lett.*, **549**, L1–L5.
- Peebles, P.J.E. (1968). Recombination of the Primeval Plasma, *Astrophys. J.*, **153**, 1–11.
- Peebles, P.J.E. and Yu, J.T. (1970). Primeval Adiabatic Perturbation in an Expanding Universe, *Astrophys. J.*, **162**, 815–836.

- Polnarev, A.G. (1985). Polarization and Anisotropy Induced in the Microwave Background by Cosmological Gravitational Waves, *Soviet Astronomy*, **29**, 607–+.
- Pryke, C. et al. (2001). Cosmological Parameter Extraction from the First Season of Observations with DASI, *Astrophys. J.*, **In Press**. astro-ph/0104490.
- Reichardt, C.L. et al. (2008). High resolution CMB power spectrum from the complete ACBAR data set. arXiv:0801.1491 [astro-ph].
- Sachs, R.K. and Wolfe, A.M. (1967). Perturbations of a Cosmological Model and Angular Variations of the Microwave Background, *Astrophys. J.*, **147**, 73–90.
- Seager, S., Sasselov, D.D. and Scott, D. (2000). How exactly did the Universe become neutral?, *Astrophys. J. Suppl.*, **128**, 407–430. astro-ph/9912182.
- Seljak, U. and Zaldarriaga, M. (1996). A Line-of-Sight Integration Approach to Cosmic Microwave Background Anisotropies, *Astrophys. J.*, **469**, 437–444.
- Silk, J. (1968). Cosmic Black-Body Radiation and Galaxy Formation, *Astrophys. J.*, **151**, 459–471.
- Smoot, G.F. et al. (1992). Structure in the COBE differential microwave radiometer first-year maps, *Astrophys. J. Lett.*, **396**, L1–L5.
- Spergel, D.N. et al. (2007). Wilkinson Microwave Anisotropy Probe (WMAP) three year results: Implications for cosmology, *Astrophys. J. Suppl.*, **170**, 377. astro-ph/0603449.
- Switzer, E.R. and Hirata, C.M. (2007). Primordial helium recombination III: Thomson scattering, isotope shifts, and cumulative results. astro-ph/0702145.
- Tytler, D. et al. (2000). Review of Big Bang nucleosynthesis and primordial abundances., *Physica Scripta Volume T*, **85**, 12–31.
- Vittorio, N. and Silk, J. (1984). Fine-scale anisotropy of the cosmic microwave background in a universe dominated by cold dark matter, *Astrophys. J. Lett.*, **285**, L39–L43.
- White, M.J. and Hu, W. (1997). The Sachs-Wolfe effect, *Astron. Astrophys.*, **321**, 8–9. astro-ph/9609105.
- Wong, W.Y., Moss, A. and Scott, D. (2007). How well do we understand cosmological recombination? arXiv:0711.1357 [astro-ph].
- Zaldarriaga, M. and Seljak, U. (1997). An all-sky analysis of polarization in the microwave background, *Phys. Rev. D*, **55**, 1830–1840. astro-ph/9609170.
- Zeldovich, Y.B. and Sunyaev, R.A. (1969). The Interaction of Matter and Radiation in a Hot-Model Universe, *Astrophys. Space Sci.*, **4**, 301–316.